5-2010

Three Dimensional Localization with Time-Gated Photon Counting and Maximum Likelihood Analysis

James Andrew Germann
University of Tennessee - Knoxville

To the Graduate Council:

I am submitting herewith a thesis written by James Andrew Germann entitled "Three Dimensional Localization with Time-Gated Photon Counting and Maximum Likelihood Analysis." I have examined the final electronic copy of this thesis for form and content and recommend that it be accepted in partial fulfillment of the requirements for the degree of Master of Science, with a major in Physics.

Lloyd M. Davis, Major Professor

We have read this thesis and recommend its acceptance:

Horace W. Crater, Christian G. Parigger

Accepted for the Council:
Dixie L. Thompson

Vice Provost and Dean of the Graduate School

(Original signatures are on file with official student records.)

To the Graduate Council:

I am submitting herewith a thesis written by James Andrew Germann entitled "Three Dimensional Localization with Time-Gated Photon Counting and Maximum Likelihood Analysis." I have examined the final electronic copy of this thesis for form and content and recommend that it be accepted in partial fulfillment of the requirements for the degree of Master of Science, with a major in Physics.

Lloyd M. Davis, Major Professor

We have read this thesis
and recommend its acceptance:

Horace W. Crater

Christian G. Parigger

Accepted for the Council:

Carolyn R. Hodges

Vice Provost and Dean of the
Graduate School

(Original signatures on file with official student records.)

Three Dimensional Localization with Time-Gated Photon Counting and Maximum Likelihood Analysis

A Thesis Presented for
the Masters of Science
Degree
The University of Tennessee, Knoxville

James Andrew Germann
May 2010

Acknowledgements

Thank you to all my family and friends who have supported and put up with me over the years.
May this work do you proud.

Abstract

The localization of particles is an important step for the study of nanoscale objects and systems. Research is ongoing on techniques to find the position of particles moving about freely or interacting with other objects, especially below the diffraction limit of optical microscopy. The method of particle localization under development here arranges four laser beam foci created from a femtosecond pulsed Ti-Sapphire laser into a tetrahedron. The microscope constructed for this thesis includes optics to split each Ti-Sapphire laser pulse into four temporally and spatially separated pulses at the focus of the objective. Maximum likelihood analysis of the time-gated fluorescence photons then provides sub-diffraction localization of single emitters. Samples of Rhodamine B, fluorescent latex beads, and nanospheres of gold are evaluated to see if they provide adequate signal-to-noise with time-gated detection for localization measurements. For these measurements, samples in aqueous solution are allowed to freely diffuse through the focal volume. Fluorescence cross correlation spectroscopy measurements indicate that the four-foci microscope is sensitive enough to detect single emitters and can also be used to measure velocity. Also, samples are dried onto microscope coverslips and translated through the focal volume of the tetrahedron using a piezoelectric stage, so that the trajectory of a single emitter is controlled. Raster scanning measurements confirm that the time-gated photon counting hardware and Labview software can separate fluorescence photons into four channels corresponding to the four excitation foci. The instrument constructed for this thesis is to be used in experiments to track and trap a single fluorescent emitter in solution.

Table of Contents

List of Figures

1. Introduction

The traditional boundary on how well a particle can be resolved in an optical microscope is the diffraction limit, the theoretical limit to the spot size of a well focused laser beam. The use of a high numerical-aperture objective can minimize the spot size to the order of a fraction of a micron, but it is not possible to resolve two particles separated by a distance smaller than the spot size. However, if it is known that there is only a single emitter, then it is possible to find the location of the emitter to a precision well below the diffraction limit. For example, in wide-field microscopy, the image of a single emitter captured on a camera is the microscope point spread function (PSF). Ideally this is an Airy function, but it can be well approximated by a two-dimensional (2-D) Gaussian function, and the center of this can be determined to an arbitrary precision limited only by the signal and noise [1].

For nanoparticle localization in 3-D, note that the axial PSF may also be approximated as a Gaussian function but it is drawn out longer than the transverse counter part. The axial PSF is not directly displayed on a CCD camera, as the camera images only one transverse plane in the sample. The 3-D PSF can be measured by recording a series of images while scanning the focus in the axial dimension, but this cannot be done very quickly. To estimate the axial position of a particle in real time, one solution is to record the size of the defocused transverse PSF at different axial distances from the emitter and then estimate the axial position by fitting the size of the observed transverse PSF image. Speidel's group did just this in 2002 with an epifluorescence microscope—by noting the distance from the center of the Airy function to the outer ring, they determined the distance of a particle from the focal plane [2].

Another method of axial localization is to create an astigmatic focus at the camera, for example, by use of a cylindrical lens in the imaging optics [3]. As the 3-D PSF is astigmatic, the size and shape of the particle image then provides a measure of the particle axial position. The astigmatic focus has the advantage of telling on which side of the focus the emitter is located.

Another conceptually straight forward method for axial localization is to split the collected light at a beam splitter and thereby image two or more focal planes at different axial depths at the same time. By simultaneously fitting the recorded images of the different focal planes, the emitter can be localized and tracked using algorithms such as the Multifocal Plane Microscopy Localization Algorithm (MUMLA) from the Ram group [4].

Another recently developed method for particle localization and tracking is to create a 3-D PSF that has a double helical pattern, by use of a spatial light modulator programmed with a phase mask pattern placed in the Fourier plane of the imaging optics [5]. The image of the particle is then two sharply focused spots. As the particle moves along the axial direction, the orientation of the two spots on the camera rotates and maps out a double helical structure, but the spots remain well focused, which provides an advantage in signal-to-noise ratio over astigmatic imaging. The position and orientation of the two spots provide localization in the *x*, *y*, and *z* axes. Look-up tables compiled from translating a stationary bead through half a rotation of the helices may be used for fast 3-D position determination [5].

Both wide-field microscopy techniques, as described above, and confocal microscopy techniques are used to observe single molecules, each with distinct advantages over the other. The wide-field methods have the ability to illuminate and observe many different molecules at once. The observed molecules can be watched in real time at frame rates limited by the camera. Contrary to the wide-field microscopy tactic of illuminating a large portion of the sample,

confocal microscopy focuses on illuminating only a small part of the sample and hence the background noise is typically much less. Thus, the signal-to-noise ratio is usually greater in confocal microscopy than in wide-field illumination microscopy. Confocal microscopy has another advantage in that it enables higher temporal resolution measurements. This is because the CCD camera is limited in its response by the read out time, which usually takes many milliseconds [6]. By contrast, the detectors used in confocal microscopy can provide sub-nanosecond time response, which enables fluorescence lifetime determinations and measurements of fast molecular processes. Finally, two-photon excitation of fluorescence, which has many advantages for intracellular imaging applications, cannot be used for wide-field illumination, but is well suited for confocal microscopy.

Several methods for particle localization with confocal microscopy have been developed. One notable method is the rotating laser spot method [7]. A sharply focused laser is translated in a circular motion about a point of interest. Through observation of the amplitude and phase of modulation of the fluorescence signal, the radial and angular components of the position of the molecule being tracked is determined [7]. The center of the circle of motion is then moved toward the molecule. The rotating spot method can be extending to tracking particles in three dimensions. To add the third dimension of tracking, the microscope objective is mounted onto a nanopositioner, which adjusts the focus back and forth between two planes. Hence, the orbiting laser beam focus scans below the fluorescent particle for a set number of rotations and then scans above the particle for the same number of rotations. Counts are separately collected for the rotations above and below the particle. The nanopositioner adjusts the microscope objective so that the particle is in the middle of the two rotation paths [8].

Another method for particle localization and tracking with a confocal microscope configuration is the four-pinhole method [9]. Instead of having just a single pinhole that defines one confocal probe volume, there are, in effect, four pinholes that define four adjacent volumes of interest. These volumes are arranged in a tetrahedron about the particle. To achieve this, a beam splitter separates the collected fluorescence into two paths that image the fluorescence collected from two different depths, and there are two adjacent fiber optic inputs, which serve as two pinholes, in each path. The distance between the centers of the two fiber optics and the optical magnification of the objective and tube lens determines the distance between the centers of the two excitation volumes in the sample. The position of the particle in 3-D is determined from the numbers of photons collected from each of the four adjacent probe volumes.

Presented in this thesis is an apparatus that uses a high repetition-rate pulsed laser for particle localization with sub-diffraction precision. The technique is similar to the four-pinhole method described above, but there is only one confocal pinhole and four excitation volumes, which are arranged in a tetrahedron. The technique avoids optical losses inherent in the four-pinhole technique [10]. The four excitation volumes also provide a means for four-beam fluorescence cross-correlation spectroscopy, which may be used to measure the velocity of fluorescent molecules in solution in 3-D.

In the introduction of this research, Chapter 2 presents background information on fluorescence correlation spectroscopy, two-photon and confocal microscopy, maximum likelihood techniques, actively quenched single photon avalanche diodes, and gold nanoparticles. Chapter 3 covers the theoretical model of the optical layout, similar to a double Mach-Zehnder interferometer, which creates the four excitation foci. Maximum likelihood analysis of the photon counts to determine the particle position is also discussed in Chapter 3. Chapter 4

describes the experimental apparatus including the optics in both the interferometer and the microscope, the piezoelectric stage with programming in Labview, the fluorescence detection and counting equipment, and how the data is analyzed. Chapter 5 reviews the data and the analysis. Chapter 6 discusses the analysis and the future goals of the setup.

2. Background

2.1 Fluorescence Correlation Spectroscopy

Through the use of a highly focused laser beam and photon counting instrumentation, it is possible to perform fluorescence correlation spectroscopy (FCS) measurements to determine equilibrium constants and other kinematic properties of a solution. FCS is a specialized version of concentration correlation spectroscopy (CCS). In CCS, the dynamic properties of the solution related to movement and particle creation are calculated via observations of particles moving into and out of a set volume [11]. In FCS, this volume is defined by the excitation region of the focused laser beam and by the confocal pinhole. Particles diffuse into and out of the excitation region and the diffusion coefficient can be determined from the mean length of the recorded fluorescence photon bursts [12]. In fluorescence cross correlation spectroscopy, there are two probe volumes, which are typically distinguished by different excitation or emission wavelengths and molecules may diffuse or be transported from one volume to the next. In the work in this thesis, the different probe volumes are distinguished by laser pulses occurring at different times together with time-gated photon detection. In general, kinematic properties of a sample can be measured from the autocorrelation function or cross correlation function of the fluorescence intensity signal(s) versus time. The value of the unnormalized auto/cross correlation for a time delay of τ is

$$G_{ij}(\tau) = \left\langle F_i(t) F_j(t+\tau) \right\rangle \quad (2)$$

$$= \lim_{T\to\infty} \left\{ \frac{1}{T} \int_0^T F_i(t) F_j(t+\tau) dt \right\} \quad , (3)$$

where $F_i(t)$ is the fluorescence from volume i at time t, and T is the total measurement time [12]. For the autocorrelation function, $i = j$. The auto/cross correlation function can be normalized by the square of the average fluorescence intensity signal(s) giving

$$g_{ij}(\tau) = \frac{\langle F_i(t) F_j(t+\tau) \rangle}{\langle F_i \rangle \langle F_j \rangle} \qquad (4)$$

$$= 1 + \frac{\langle \delta F_i(0) \delta F_j(\tau) \rangle}{\langle F_i \rangle \langle F_j \rangle} \quad , \qquad (5)$$

where $\delta F_i(t)$ is the fluctuation of the fluorescence from the average fluorescence signal from volume i at time t, i.e.,

$$\delta F_i(t) = F_i(t) - \langle F_i \rangle . \quad (6)$$

In Eqn. (5), $t = 0$ as the time between fluctuations is the important factor here. If only the fluorescence fluctuations are considered, Eq. 5 can be simplified further to

$$g'_{ij}(\tau) = \frac{\langle \delta F_i(0) \delta F_j(\tau) \rangle}{\langle F_i \rangle \langle F_j \rangle} . \qquad (7)$$

2.2 Two-Photon and Confocal Microscopy

In FCS experiments, the fluctuations of fluorescence provide information about the system, but for fluctuations to be observable the excitation volume needs to have a small number of emitters, typically 0.1—5. Confocal microscopy typically produces a probe volume on the order of ~0.02—2 femtoliters through the use of a pinhole and thereby gives an appropriate number of emitters for nanomolar solution concentrations. An example of a setup for a confocal microscope, which was used in intial experiments for this thesis research, is shown in Figure 1.

Fluorescence collected from the sample by the microscope objective is focused to a pinhole, which blocks out of focus light.

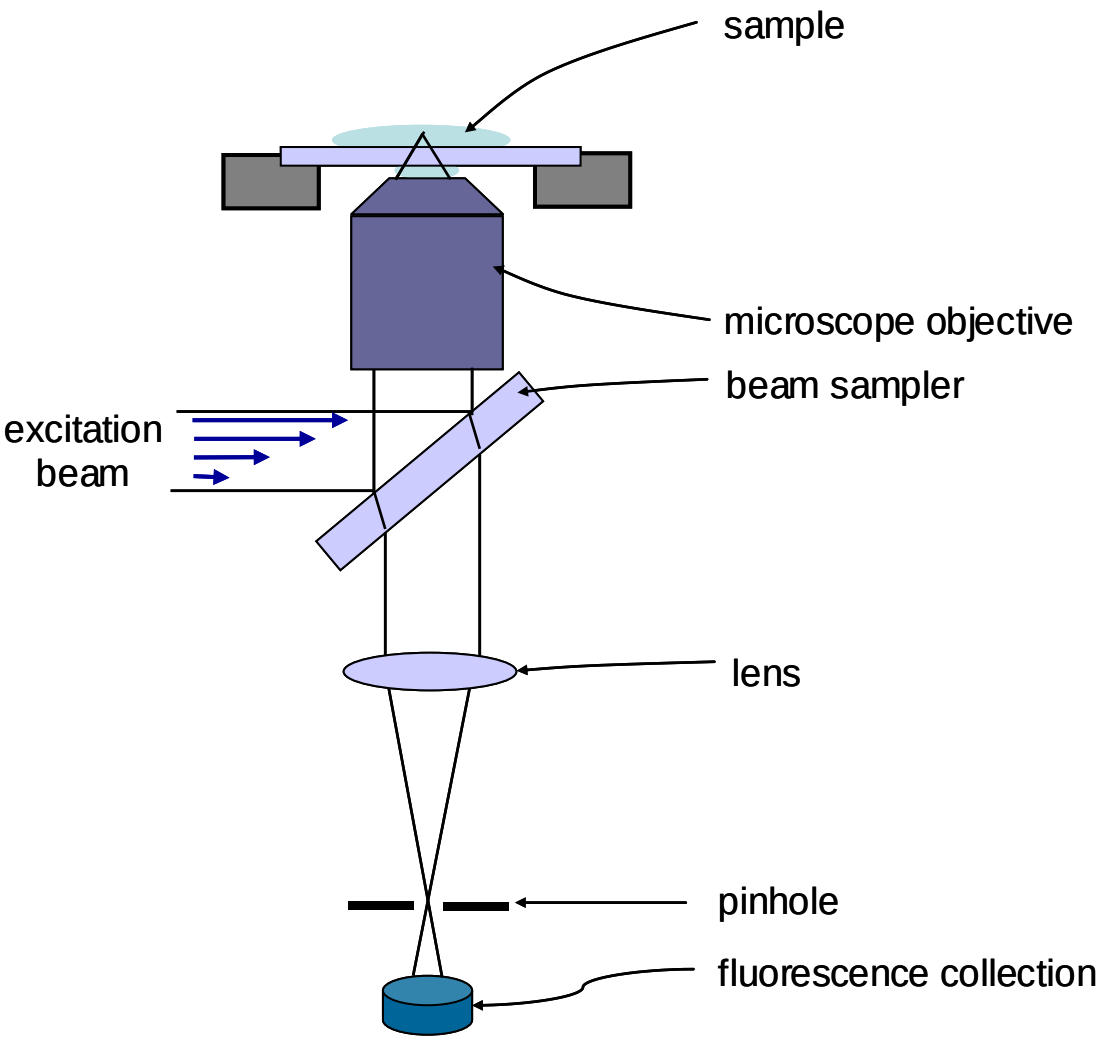

Figure 1. An example of a confocal microscope.

Rather than a linear dependence seen in one-photon experiments, the fluorescence count rate in a two-photon experiment has a quadratic dependence on the excitation power [13], i.e.

$$F(t) \approx \alpha \int dV I^2(\vec{r},t) C(\vec{r},t) . \quad (8)$$

For Eq.8, $F(t)$ is the fluorescence signal at time t, α is a constant representing the net fluorescence excitation and detection efficiency, I is the laser excitation irradiance, and C is the concentration [14]. The laser irradiance near the focus can be represented with a Gaussian-Lorentzian model (Eq.9 [14])

$$I(\vec{r},t) = \frac{2I_0 w_0^2}{\pi w^2(z)} \exp\left(-\frac{2r^2}{w^2(z)}\right) \quad (9)$$

where

$$w^2(z) = w_o^2\left(1+\left(\frac{z}{z_0}\right)^2\right) \quad (10)$$

and

$$z_0 = \frac{\pi w_0^2}{\lambda} \quad (11)$$

are the beam size and the Rayleigh range (Eq.11) respectively, I_0 is the irradiance at the focus, w_0 is the beam waist (i.e., the beam size at the focus), r is the radial distance from the optical axis, z is the distance along the optical axis, and λ is the wavelength [14]. Two-photon excitation has many advantages. The quadratic dependence on excitation limits the emitters to those in the focus, creating a confocal volume without the use of a pinhole. Because the emitters tend to excite in the focus in two-photon excitation instead of throughout the sample, as in one-photon excitation, the amount of photobleaching in the sample is kept to a minimum [15]. Fluorescence trends can be seen in Figure 2, which compares one-photon and two-photon excitation. There is also a tolerance of wideband filters in two-photon microscopy because of the large shift between

the excitation and fluorescence wavelengths. In biological samples, ultraviolet light can be replaced with infrared light, which has a deeper penetration depth and is less harmful to organic samples [13,15].

There are two disadvantages to the two-photon method of imaging. To get the same amount of fluorescence in a two-photon excitation experiment typically requires more laser power than in the one-photon counterpart, e.g., a one photon excitation requiring 50—100 μW would require 5—10 mW to get the same result in a two-photon procedure. Two-photon excitation requires pulsed laser excitation and in this case (with either one- or two-photon excitation) the maximum fluorescence signal achievable when the excitation is saturated depends on the repetition rate of the laser [13]. This last disadvantage can be easily remedied by artificially increasing the laser repetition rate, such as adding a second arm to the beam path or a second laser with the same repetition rate but delayed by half the pulse period.

Figure 2. Two-photon excitation (top) and one-photon excitation (bottom) in a sample of laser dye. Image provided by http://belfield.cos.ucf.edu/one%20vs%20two-photon%20excitation.html

2.3 Maximum-Likelihood Estimation

Maximum-likelihood estimation (MLE) is used to analyze the data received from the four-foci experiment. MLE has the advantages of being sufficient, consistent, efficient, and parameterization invariant [16]. Many of the estimation methods used in statistics are based on the MLE method. MLE takes into account the particular statistical distribution of the data and hence provides a considerable advantage over the least-squares method, which implicitly assumes Gaussian-distributed data. Also, the least-squares method has no rigorous basis for testing hypotheses or constructing confidence intervals [16], whereas these are possible with MLE.

The MLE method begins by finding a model expression $L(x_i \mid w_i)$ for the conditional probability (i.e., the likelihood) to get the measured data set x_i, given that the model parameters take certain values, w_i. The parameters w_i are the quantities to be estimated. The parameters are then adjusted until the maximum possible likelihood function is found. This may be achieved by finding the partial derivatives of the likelihood function with respect to each of the parameters and setting them equal to zero; $\partial L(x_i \mid w_i)/\partial w_j = 0$. In many cases, including in this work, it is computationally faster to find the parameters that maximize the natural logarithm of the likelihood function.

2.4 Single Photon Avalanche Diodes –SPADS

In the past twenty years, there has been an advance in the detection and quantification of fluorescence emission. Single photon avalanche diodes (SPADs) have become a popular choice for photon detection and have largely replaced the previous technology, photomultiplier tubes.

SPADs are smaller, more robust, and run on lower voltages [17]. The photodiode p-n junction is reverse biased above the breakdown voltage. When a photon hits the active area of the detector, an electron-hole pair is created. From this initial electron-hole pair, an avalanche current is created. The avalanche current must then be quenched, either passively or actively. With passive quenching, a large (~100 kΩ) resistor is placed in series with the SPAD so that the current through the resistor is unable to sustain the avalanche. Hence the avalanche stops once the stray capacitance of the device is discharged. Then the current through the resistor lets the bias build up slowly until the capacitance of the device is recharged. The bias can take microseconds to restore, which can give a count rate dependent tail to the prompt [17]. The other method of quenching is active quenching, in which active transistor components in the circuit quickly lower the bias when they detect an avalanche current and then quickly raise it above the breakdown potential again. For actively quenched detectors, the dead time is typically on the order of tens of nanoseconds [17]. The fraction of photons not counted by the SPAD is $1-e^{-RD}$, where R is the theoretical count rate (s^{-1}), and D is the dead time of the SPAD (s).

2.5 Fluorescent Samples

The samples described below were prepared and diluted to the appropriate nanomolar/picomolar concentrations with ultrapure water (Barnsted International, Nanopure UV). Also, to maintain low background photon counts, ultrapure water from a clean vial delivered with a micropipette with disposable tips was used for the microscope water immersion objective.

2.5.1 Gold Nanoparticles

Gold nanoparticles are a popular choice among fluorescent probes today because of their resistance to blinking and photobleaching [18]. Gold nanoparticles also have the advantage of being inert in most biological systems, they are easily attached to biological molecules such as amino acids and nucleotides, they provide especially strong emission compared to the background noise, and they are commercially available in various diameters under the trade name Nanogold [18]. Their useful properties derive from the large density of free electrons and the susceptibility of these free electrons [19]. Gold nanoparticles both scatter and absorb light efficiently, but depending on the size of the nanoparticles, scattering or absorbing is more efficient [19]. For particles below 100 nm in diameter, the main focus is on absorption [19]. To maximize the absorption of these particles, excitation wavelengths close to the plasmon frequency should be used [19]. The gold nanoparticles used in this work have diameters of only about 1.4 nm. Such particles have been reported to provide a strong fluorescence signal when close to a surface [20].

2.5.2 Rhodamine B

Rhodamine B is a highly fluorescent molecule, which is used as a laser dye and which has a higher two-photon excitation cross section than most other dyes. Previous two-photon experiments have been conducted with Rhodamine B, especially the mapping of the effective cross section and two-photon excitation spectrum as seen in Figure 3 [21]. For the excitation spectra the maximum fluorescence intensity is generated with 700 nm light [21], which is a blue shift from the expected 1085.5 nm. Rhodamine B has a maximum at 542.75 nm in one-photon absorption. Another peak cross section point is located at 820 nm, which is close to the 800 nm excitation wavelength provided by the Ti-sapphire laser used in this experiment. The emission

spectrum of Rhodamine B under a two-photon process is identical to that of a one-photon process [21].

2.5.3 Latex Beads

Another popular choice of fluorescent label is the latex bead. Latex beads are considerably larger than single dye molecules and range in size from tens of nanometers to a few microns. They have multiple fluorescent molecules on them, allowing the beads to be very bright. As with the Rhodamine B, there should be a blue shift in the theoretical two-photon excitation wavelength and no change in the fluorescence wavelength.

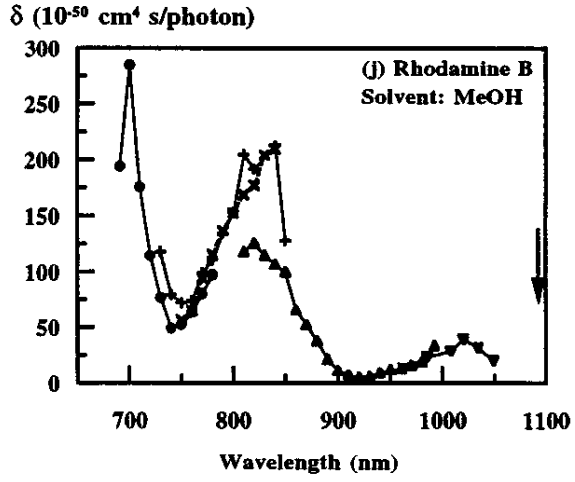

Figure 3. Excitation spectrum of Rhodamine B.

3. Theory

3.1 Double Mach-Zehnder Interferometer and Microscope Setup

To create the four excitation regions for particle localization, an optical system based on the Mach-Zehnder interferometer is used to spatially and temporally separate a single laser beam to produce four foci, as shown in Figure 4. To temporally separate the four output pulses, the interferometer introduces four beam paths. The main or direct path yields the shortest time for light to travel from the first beam splitter to the microscope objective. The side paths are a particular length longer than the direct path to introduce a time delay of one-half the laser pulse period and one-quarter of the pulse period. For the 76 MHz repetition rate laser pulses used in the experiment, the pulse period is 13.2 ns (1/76 MHz). The additional length can be determined by using the equation

$$d = \frac{c}{t}, \qquad (13)$$

where d is the desired path length, t is the desired time delay, and c is the speed of light. Hence with the 76 MHz pulsed laser, the pulses arrive 3.3 ns, 6.6 ns, and 9.9 ns after the first pulse arrives at the objective. Then, 3.3 ns after the last pulse arrives, the first pulse of the next set arrives.

Spatially separation of the pulses is an exercise of tilting and translating the mirrors and beam splitters in the interferometer, which is done in the four steps, α, β, γ, δ, as shown in Figure 4. The four foci start off in the same place in space. To separate the one focus to two requires translating (step α) and tilting (step β) the second beamsplitter (labeled bs2 in Figure 4) until the foci due to paths A1 and B2 are separated from those due to paths B1 and A2. The mirrors

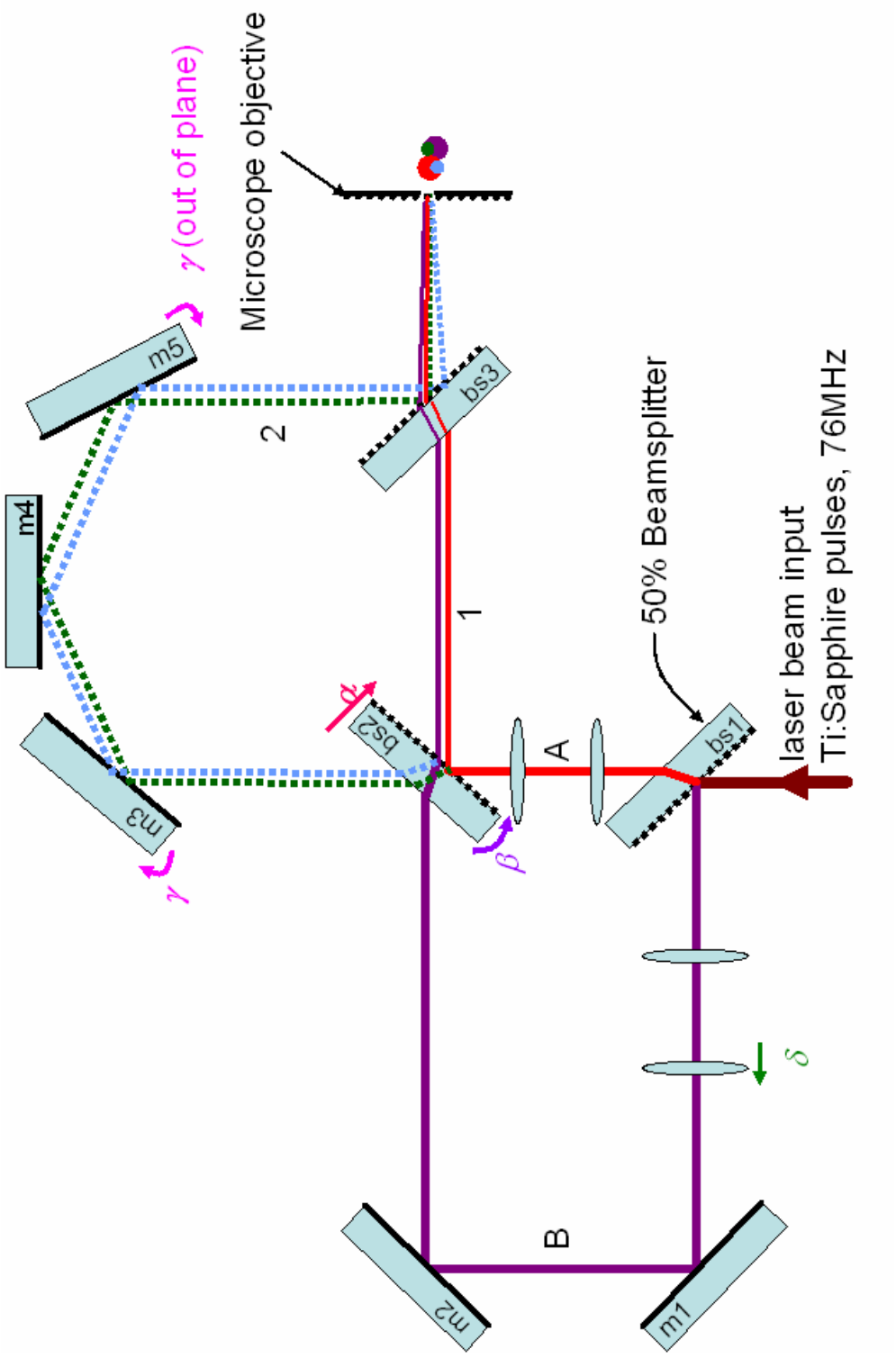

Figure 4. Layout of double Mach-Zehnder interferometer.

labeled as m3 and m5 in the diagram are then tilted out of plane (step γ) to separate A2 from B1 and B2 from A1. This gives four foci all in the same plane. Adjustment of the lens in the arm marked B in the figure (step δ) moves the focus toward or away from the objective, thus raising the foci B1 and B2 to a new focal plane. The final shape of the tetrahedron is shown in the bottom left panel of Figure 5. The foci that travel through the A-arm of the interferometer act as an axis on the bottom, while the foci that travel through the B-arm form the top axis. To form the axis that runs parallel to the optical axis of the objective, the combined foci on the bottom and the combined foci on the top serve as points on the "z"-axis. Because of the nature of two-photon excitation, as explained in section 2.1, the probability of molecules fluorescing through the sample is low except at that focus. Thus the shifting of one pair of foci, or an equal shift of both foci in opposite directions, will allow for *z*-axis sensitivity.

After the double-interferometer optics, the four beams enter the fluorescence microscope, which is shown schematically in Figure 6. Within the microscope, the laser light is reflected from a Ti-Sapphire mirror and into a high numerical aperture objective. The fluorescence is collected by the same objective and is directed through the Ti-Sapphire mirror. As mentioned in Section 2.2, the large difference between the excitation and fluorescence wavelengths easily allows a dichroic mirror, such as the Ti-Sapphire mirror, to separate fluorescence from reflected excitation light. The beam of fluorescence is then focused with a lens onto a CCD camera, or through a pinhole and onto a SPAD detector. The pinhole here serves to limit the light collection to a comparatively large volume containing the entire tetrahedron formed by the four foci, rather than define a small confocal volume. Details on the experimental implementation of the double-interferometer set up and the microscope are given in Sections 4.1 and 4.2.

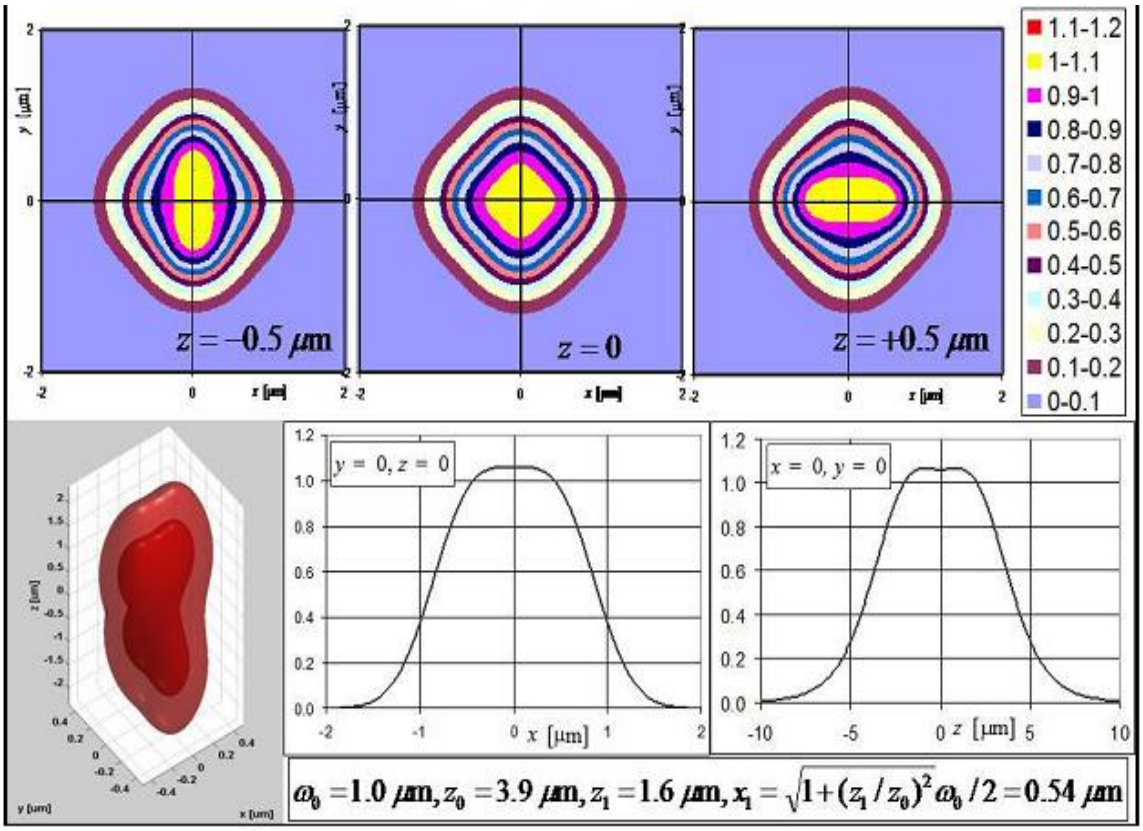

Figure 5. Model of the four-foci excitation layout. The top three pictures are slices of the intensity profiles of the tetrahedron perpendicular to the objective axis. Bottom center and bottom right are intensity versus position perpendicular to the objective axis and parallel to it respectively. Bottom left is a three dimensional view of the four foci arranged in the tetrahedral pattern [14].

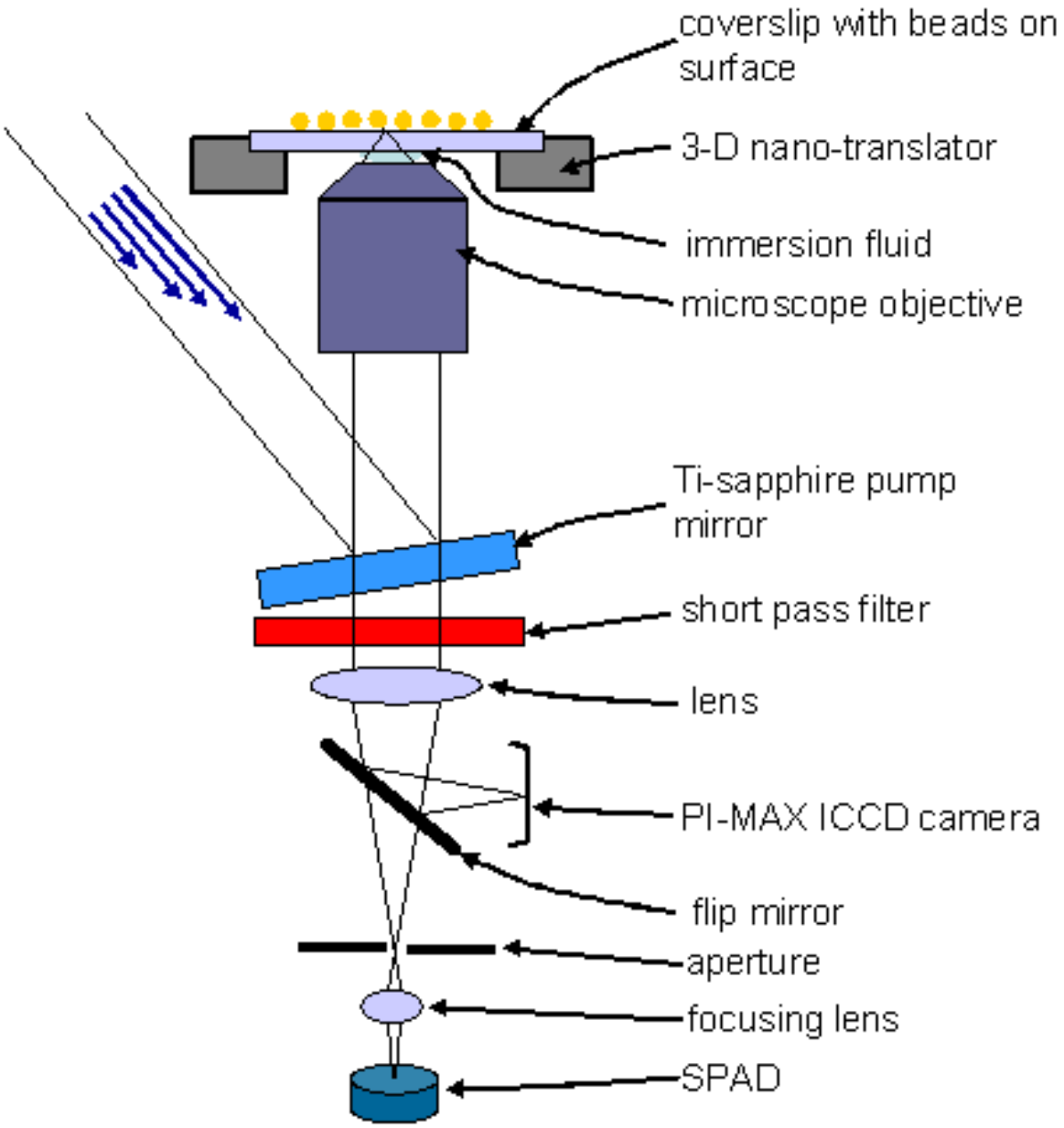

Figure 6. Layout of fluorescence microscope. The excitation beams arrive from the upper left and reflect off the Ti-Sapphire mirror into the objective. The fluorescence passes through the objective and is detected by either a camera or a SPAD.

3.2 Maximum-Likelihood Position Determination with Four Beams

The signals from the SPAD in Figure 6 are directed to a system for time-resolved photon counting, which separates the photon counts into four bins that correspond to the four time-delayed foci. Details on the photon counting electronics are given in Section 4.4. An experimental time-spectrum of the photon counts from scattered light, obtained without the short-pass laser-blocking filter (see section 4.2), is shown in Figure 7 and is used to explain the theory of the time-gated detection. As seen in Figure 7, if a photon arrives between the A1 pulse and the A2 pulse, it is placed in the bin associated with A1. A photon arriving in between pulses B1 and B2 is attributed to bin B1, which similarly corresponds to the previous focus, as the focus B1 is that which most probably gave rise to the photon.

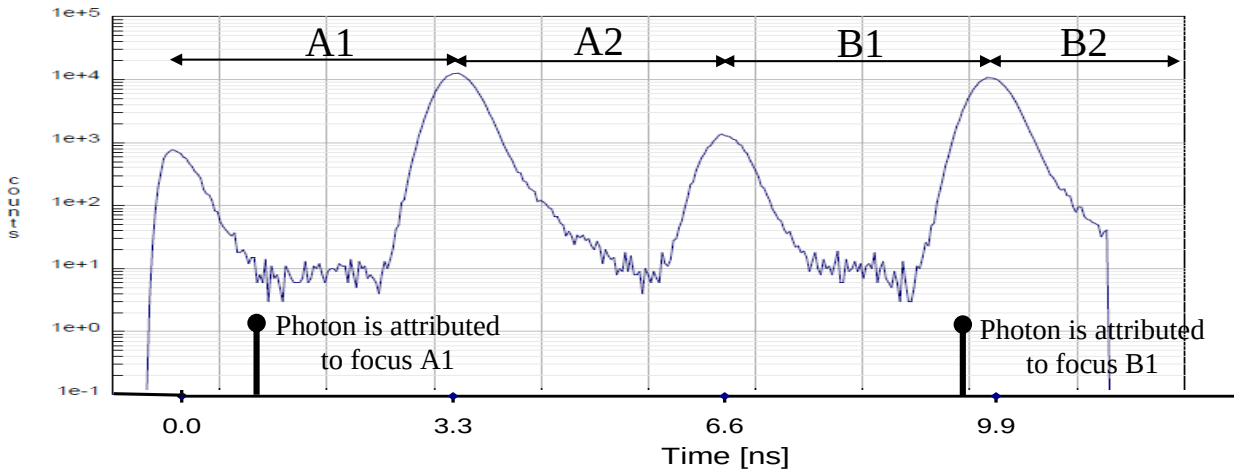

Figure 7. Time spectrum of four beams arriving at the SPAD.

Once the total numbers of photons in each of the four time bins N_1, N_2, N_3, N_4 are known, maximum likelihood analysis is used to determine the position of the fluorophore. The conditional probability to detect N_1, N_2, N_3, N_4 photons in the four time bins if the particle is at position $\mathbf{r} = x, y, z$ is given by the multinomial distribution:

$$\text{Prob}(N_1, N_2, N_3, N_4 \mid \mathbf{r}) = \frac{N!}{N_1! N_2! N_3! N_4!} p_1(\mathbf{r})^{N_1} p_2(\mathbf{r})^{N_2} p_3(\mathbf{r})^{N_3} p_4(\mathbf{r})^{N_4}, \qquad (14)$$

where $N = N_1 + N_2 + N_3 + N_4$ is the total number of photons collected, and $p_i(\mathbf{r})$ is the probability that a detected photon from a molecule at position $\mathbf{r}$ will fall into bin *i*.

The probabilities $p_i(\mathbf{r})$ may be measured in calibration experiments in which photons are collected into the four bins from a particle at a known location $\mathbf{r}$. They may also be determined theoretically as

$$p_i(\mathbf{r}) = \frac{\sum_{j=1}^{4} \alpha_{ij} F_j(\mathbf{r})}{\sum_{j=1}^{4} F_j(\mathbf{r})} \qquad (15)$$

where $F_j(\mathbf{r})$ is the fluorescence count rate due to beam *j* from a particle at position $\mathbf{r}$, and α_{ij} is the probability that a photon excited by beam *j* will fall into bin *i*.

4. Experimental Methods

4.1 Optical Layout of Double Mach-Zehnder Interferometer

The laser system used in this work consists of a femtosecond Titanium-sapphire laser (Spectra-Physics, Tsunami), pumped by a continuous wave 532 nm laser (Coherent, Verdi). The Ti-sapphire laser emits a continuous train of ~140 fs pulses at 76 MHz, with a center wavelength of ~800 nm. The path that the near-infrared pulses take is covered in Section 3.1. The beam splitters used in this experiment (Newport model: 10RQ00UB.2) are designed for ultrafast femtosecond laser pulses and produce a 50/50 split for *s*-polarized light for wavelengths of 700-950 nm. The stock mirrors used in this experiment are made of silver to provide high reflectivity while maintaining low dispersion. The lenses found in paths A and B are plano-convex singlets with focal lengths of 50 mm and 100 mm and were initially placed in a Keplerian beam expander configuration to double the laser beam size. The lenses selected were stock lenses already found in the lab. The path length of the 2 arm is ~1 m longer than the 1 arm and the length of the B arm is ~2 m longer than the A arm. The position and tilt of bs2 and the tilt of mirrors m3 and m5 were adjusted as described in Section 3.2 until the four foci were appropriately positioned. As shown in Figure 5, the desired positions are such that the spots are largely overlapping. The position of each of the four foci was observed by imaging the light reflected from the surface of the coverslip with the CCD camera (Andor iXon EMCCD), as shown in Figure 8. In order to adjust the separation of the lenses in step δ of Figure 4, the coverslip was translated along the optical axis (*z*-axis) to the desired focal position for the two spots of paths B1 and B2, and lens separation adjusted to bring the images of the two spots into sharpest focus. A photograph of the

final experimental setup is shown in Figure 9. Visible in this photograph is the Helium-Neon laser (beam path indicated by dashed line), which is essential for initial alignment of the optics.

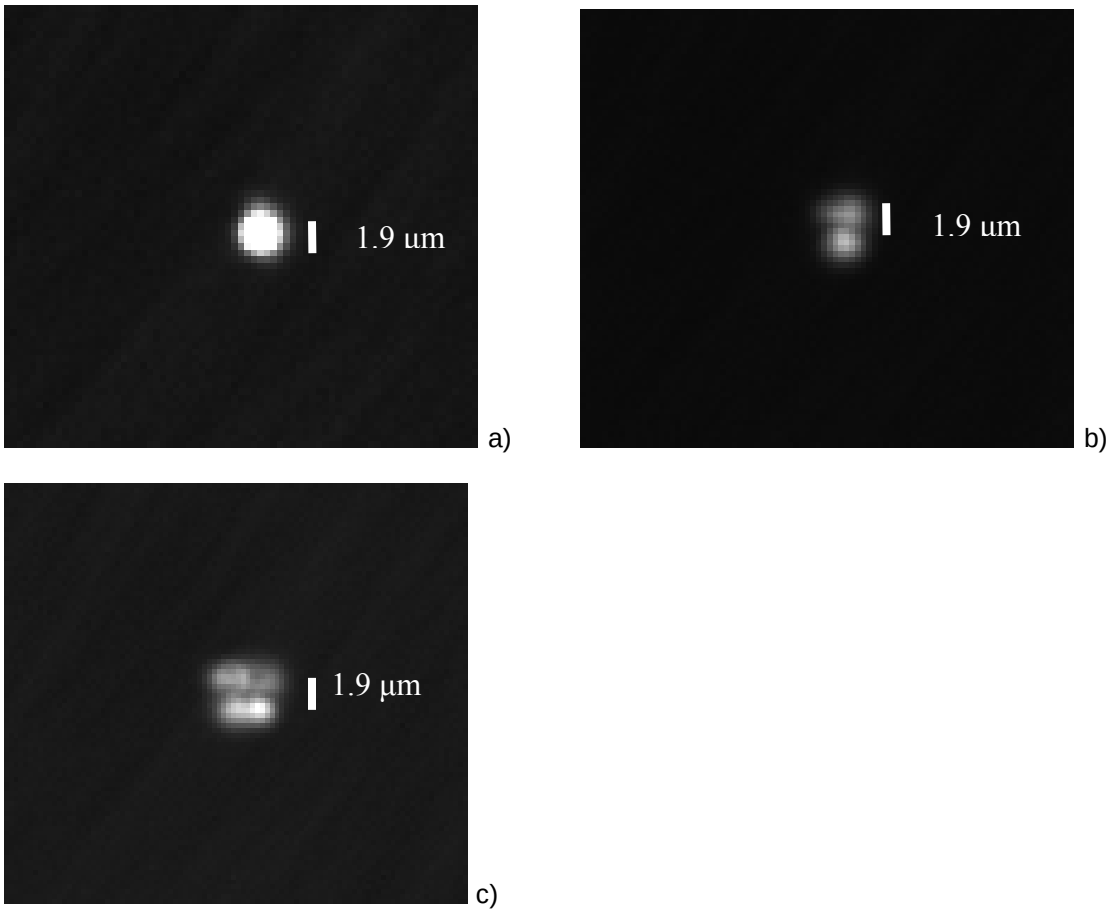

Figure 8. The formation of the excitation volumes. Starting from one spot (a) the second beam splitter is translated and tilted until there are two spots (b). From two spots the mirrors in the 2-arm are tilted out of plane until there are four spots (c).

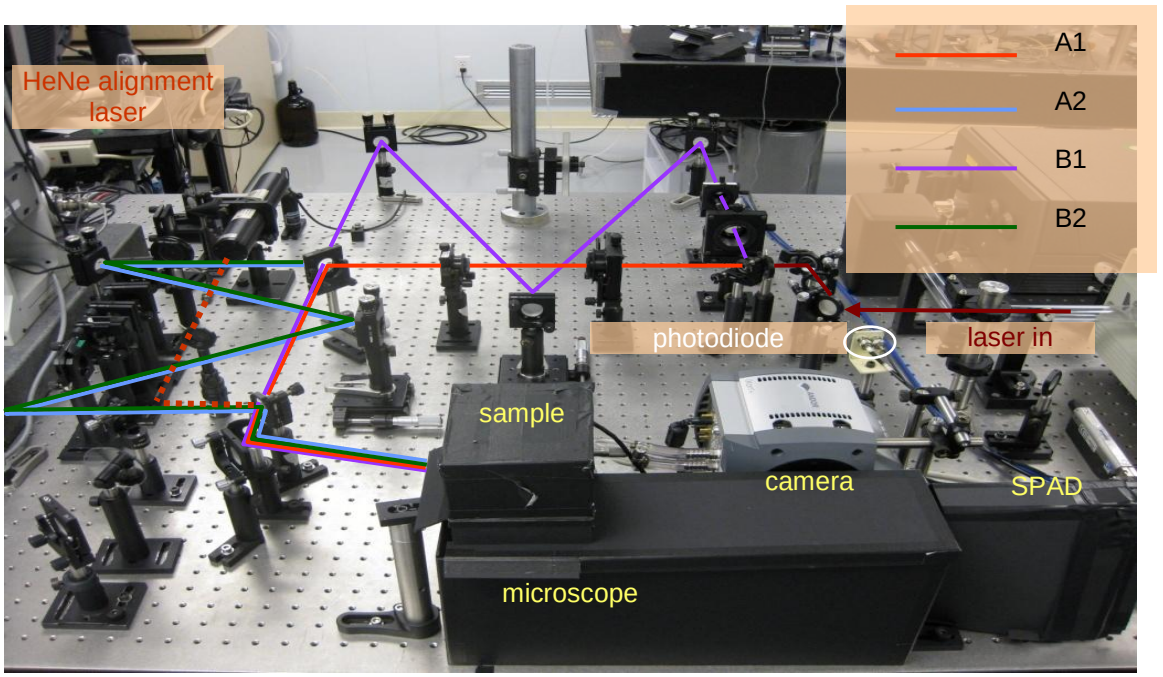

Figure 9. Photo of experimental set-up with optical paths of beams highlighted.

4.2 Optical Layout of Microscope and Fluorescence Collection

Figure 6 shows a schematic of the optical layout of the microscope. A Ti-Sapphire pump mirror (Newport 10B20UF.20) is used as a dichroic mirror within the microscope to reflect the laser beams toward the objective. The objective used here is a water immersion objective with numerical aperture NA=1.2 (Olympus UPLSAP060XW, catalog 1-U2B893). The objective focuses the laser beams very tightly to promote two-photon excitation within the sample. Fluorescence from the sample is collected by the same objective and passes through the Ti-Sapphire mirror. The fluorescence then passes through a 150 mm plano-convex singlet lens, and through a short-pass interference filter (Omega Optical, 3RD660SP) to further attenuate reflected laser wavelengths, and is focused through a 300 micron pinhole. The objective has a magnification of 60 × when used in an Olympus microscope with a tube lens with focal length of 180 mm. With the use of the 150 mm focal length lens, the magnification is 50 ×. Hence the 300 micron pinhole defines a collection region with diameter of 6 microns in object space, which, as mentioned at the end of Section 3.1, is larger than the region defined by the two-photon fluorescence excitation of the four foci.

After the pinhole, the fluorescence is then focused onto a SPAD and photons are counted. Alternatively, a mirror may be placed in front of the pinhole to focus the light onto the CCD camera. Alignment of microscope components was done with the aid the Helium-Neon laser, as the filters block out nearly all reflected near infrared beams. Photographs of the final setup of the microscope are shown in Figure 10 and Figure 11.

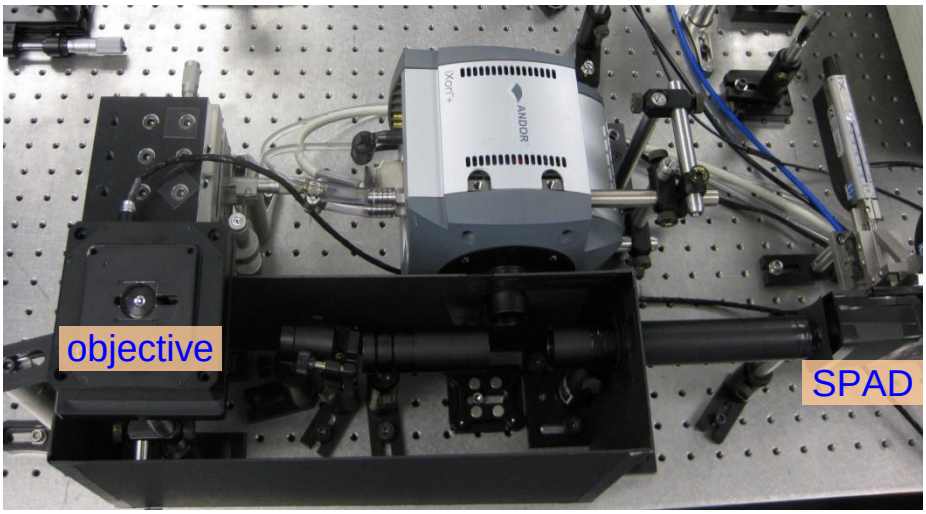

Figure 10. Top view of objective, piezoelectric stage, camera, SPAD, and other optics.

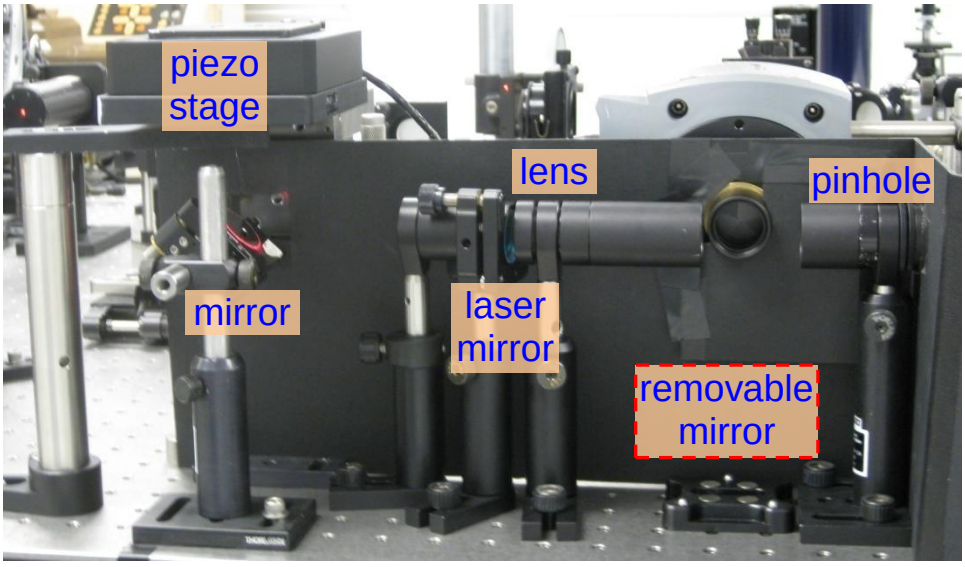

Figure 11. Side view of objective, piezoelectric stage, camera, SPAD, and other optics.

4.3 Piezoelectric Stage

A piezoelectric stage is used to move the sample in relation to the objective. The piezoelectric stage used in this setup was a P-733.3DD model from Physic Instrumente and the controller unit used to communicate with the stage was the E-710 model from Physic Instrumente. The P-733.3DD model has a movement range of 30 μm in both the *x*- and *y*-direction, the direction perpendicular to the optical axis of the objective, and 10 μm in the *z*-axis, the direction parallel to the optical axis of the objective, and hence it was mounted on a 3-axis manual translation stage (Newport 561-xyz with DM-13 differential micrometers). The E-710 controller communicates with the computer via a RS-232 cable. Two Labview programs were created in order to manipulate the stage— a raster scanning program and a joystick program. A short description of these programs is provided below.

4.3.1 The Raster Scanning Program

The Raster scanning program uses the wave generator feature of the piezoelectric stage controller. The Labview program reads in the desired scanning range in *x* and *y*, the desired width between passes, and the desired velocity, and it sets up three waves in the controller. At the end of each pass, the controller sends out a TTL pulse to the photon counting data acquisition electronics, to signal that it has reached the end of the line and is starting the next.

4.3.2. The Joystick Program

The Joystick program uses the absolute move command to move the piezoelectric stage a certain distance in any direction up to the physical limits of the stage. The step size of

movement can be as large as 1 μm or as small as 1 nm. Sliders are also provided for quick movement to a desired area. The current position of the piezoelectric stage with relation to the stage's home position (x=0, y=0, z=0) is provided with numerical indicators.

4.4. Photon Detection

The fluorescence photons can be detected with either of two devices, the CCD camera or the single photon avalanche diode (SPAD), which outputs a TTL pulse for each detected photon. To change between the two devices, a mirror mounted on a magnetic base can be placed in the beam path or removed from it. The camera used in this experiment is the iXon EM + DU-897 model produced by Andor. It has an imaging area of 512 × 512 pixels and takes an image every 30 ms (refresh rate of 33.3 Hz). The camera is cooled by a thermoelectric cooler and with a water cooling system to an operational temperature of –70°C.

The SPAD used in this experiment is the SPCM-AQR-13 model from Perkin-Elmer. This model of SPAD is actively quenched (Section 2.4), has a dark count rate of ~300 s^{-1} and an active area of ~150 μm diameter. The fluorescence collected from the sample is focused onto the center of the active area using a 10× microscope objective. The SPAD is positioned to place the active area in the focus of the objective using a 3-axis manual translation stage (Newport 461-xyz).

The TTL pulses from the SPAD are counted using a National Instruments PCI-6602 counter-timer card in the computer and are also passed to a card for time correlated single photon counting (TCSPC) (PicoQuant TimeHarp 200, used with PicoQuant PRT-400 router). The TTL pulses routed to the TimeHarp 200 card are recorded in Time-Tagged Time-Resolved (TTTR)

mode, which records a time stamp indicating arrival of the TTL pulse. Pulses are tagged with a 12-bit number that indicates the micro-time between the photon detection and the subsequent laser excitation pulse, which is in the range 0—13.2 ns, and also a 16-bit number that indicates the macro-time of the photon arrival with respect to an internal 100 MHz clock. To indicate when to stop the micro-time cycle, an ultrafast beam sampler (Newport 10B20-01NC.2) is positioned prior to the double interferometer and reflects part of the Ti-Sapphire beam onto a fast photodiode. The photodiode, marked in Figure 9, is connected to the stop input of the TimeHarp 200 by a 50 Ohm cable with appropriate delay length. Photon count records are analyzed post collection with the Labview program "mainCorr" (previously developed by Lloyd Davis) to find the cross correlation functions of photons from four selected time bins

4.5 Data Collection and Analysis

4.5.1 FCS Measurements

A sample of 10.3 nM Rhodamine B was placed on top of a quartz coverslip over the microscope objective. One beam of the double Mach-Zehnder interferometer was allowed into the objective. The sample of Rhodamine B was excited and the fluorescence photons were detected with the SPAD. The autocorrelation function was calculated using the measured photon counts and the LabView program "Correlator" (previously developed by Lloyd Davis). After all four arms were measured separately, the autocorrelation function of the fluorescence signal from all four beams together was calculated with the Correlator program. The four beam FCS measurements were repeated with orange latex beads. The laser power of the combined four beams was attenuated at 30 mW, 20 mW, 10 mW, and 5 mW. The Correlator program was used to determine if the signal-to-noise ratio was large enough to show photon bursts from particles entering and exiting

the focus of the beam. Fluorescence count levels were carefully monitored to safeguard the SPAD.

4.5.2 Time Spectrum Measurements

The fluorescence decay time spectrum of the three potential fluorophores was recorded using the PicoQuant TimeHarp 200 card. A sample was placed on a quartz coverslip and three of beam paths were blocked to enable the use of only one focus. Fluorescence was collected using the SPAD and photon time-stamps recorded with the TimeHarp.

4.5.3 Fluorescence Measurements with Four Foci and Time-Gated Photon Counting

A 1 nM concentration of sample diluted in water was placed on top of a quartz coverslip and all four beams paths were unblocked. Particles were allowed to freely diffuse through the combined excitation volume. The power of each beam was adjusted to 5 mW before entering the microscope box. Fluorescence was counted with the SPAD and incoming TTL pulses were time-stamped in TTTR mode. Photons were separated into four bins corresponding to the four excitation volumes based on the arrival time of the TTL pulse. FCS and FCCS analysis was applied to the photon counts.

To further test the tetrahedron, a single gold nanodot was translated through the excitation volume using the Raster Scanning program and piezoelectric stage. Individual gold particles were first found using the raster scanning program with the Labview vi, “Ccorrelator”. A single gold particle traversing the excitation volume will produce a Gaussian shaped photon burst pattern as shown in Figure 12. When a single gold particle is found, the raster scanning program was run again but data was collected with the TimeHarp hardware and software.

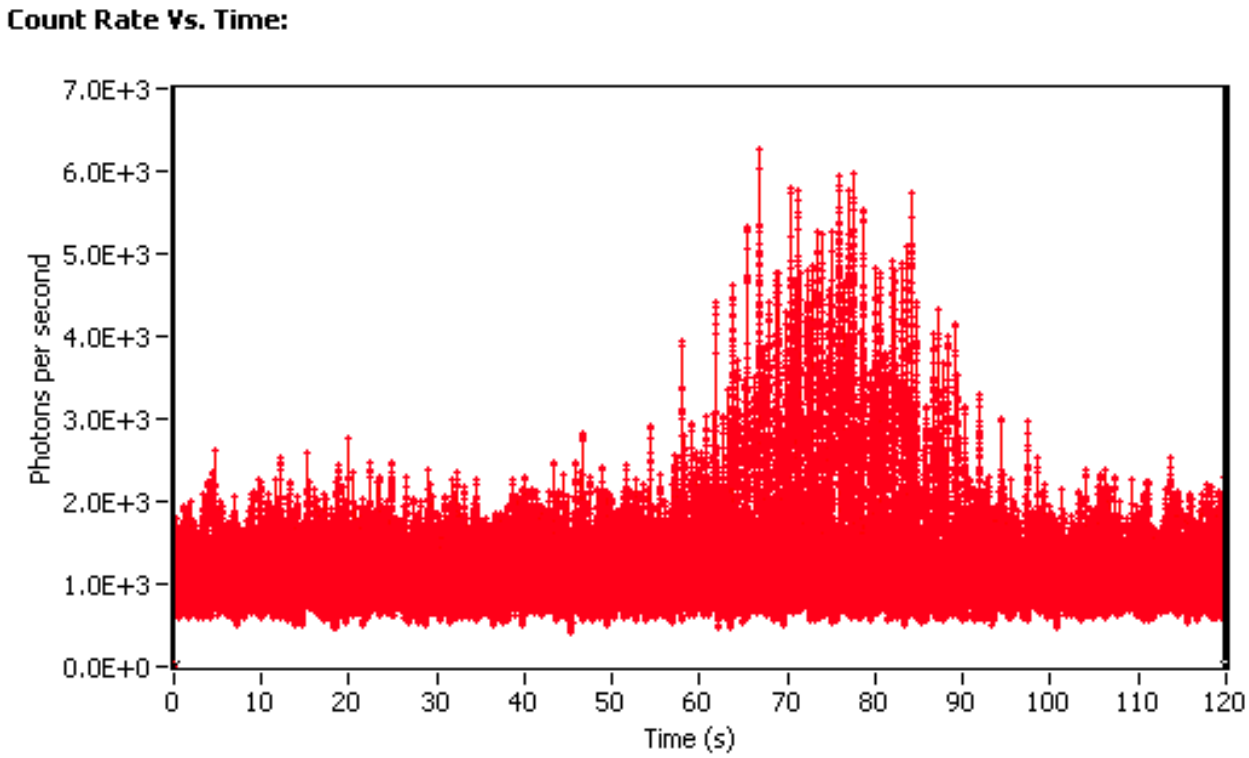

Figure 12. Count rate vs. time for Nanogold raster scanning across a single focus

5. Experimental Results

5.1 FCS Results

FCS measurements were taken for Nanogold, orange fluorescent beads, and Rhodamine B using the procedure described in Section 4.5. The orange fluorescent beads had a very strong signal-to-noise ratio and a large autocorrelation amplitude as shown in Figure 13. The Rhodamine B had a sufficient two-photon signal-to-noise ratio to have a peak in the autocorrelation function, but it was less than that of the orange fluorescent beads and the autocorrelation had a smaller peak amplitude, as shown in Figure 14. The Nanogold in solution gave no discernable signal, as seen from the autocorrelation function graphed in Figure 15, which remains flat with amplitude of 1.0 (except for noise). However, on the surface of fused silica, the Nanogold particles were very bright, as seen by the count rate plot in Figure 16.

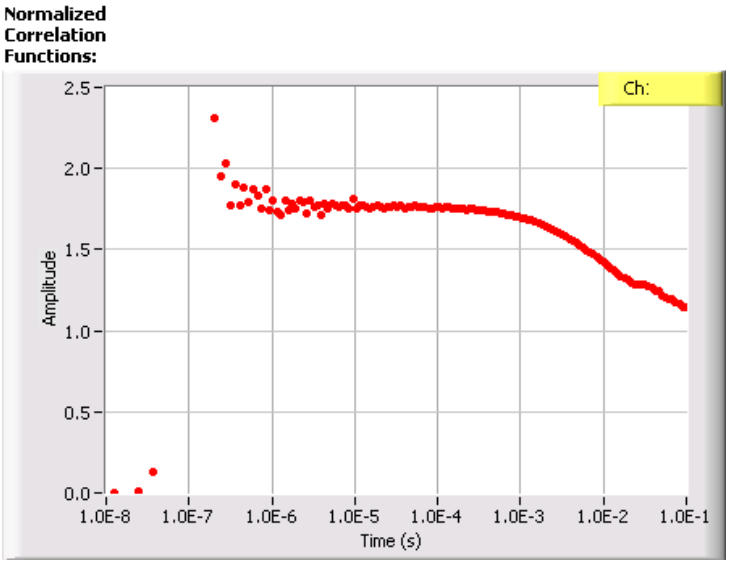

Figure 13. Autocorrelation Function of Latex Beads

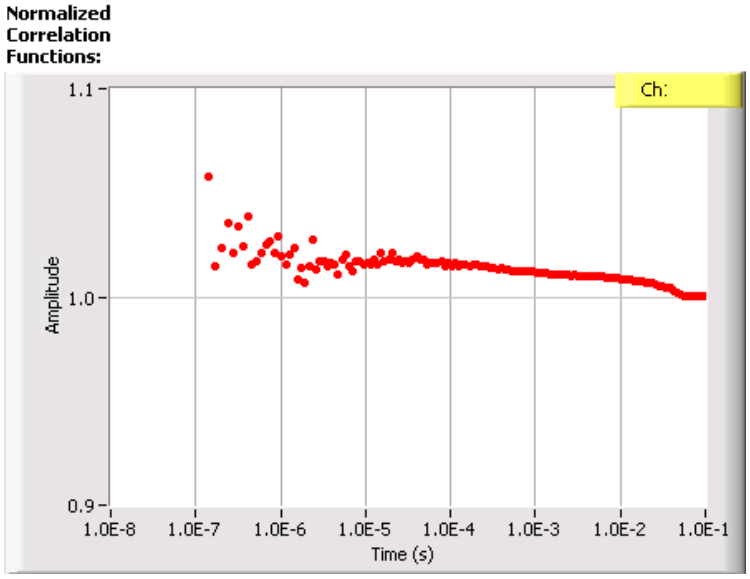

Figure 14. Autocorrelation Function of Rhodamine B

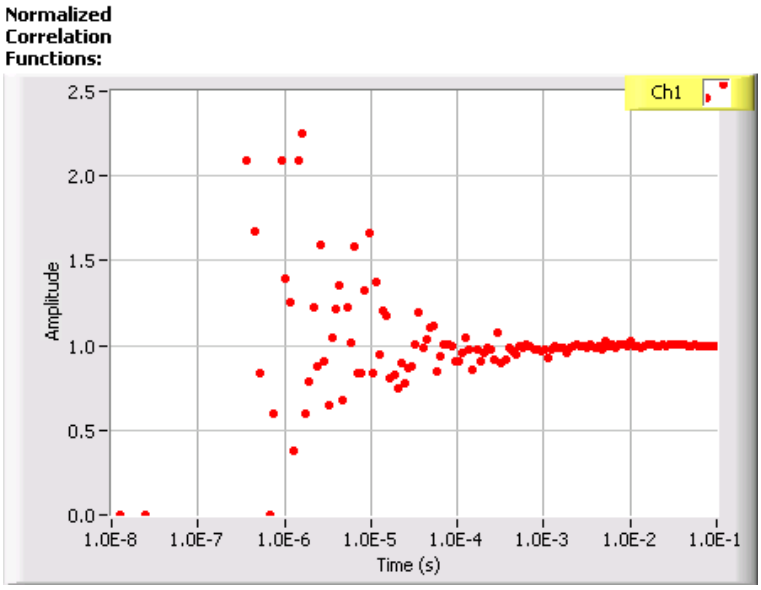

Figure 15. Autocorrelation Function of Nanogold in Water

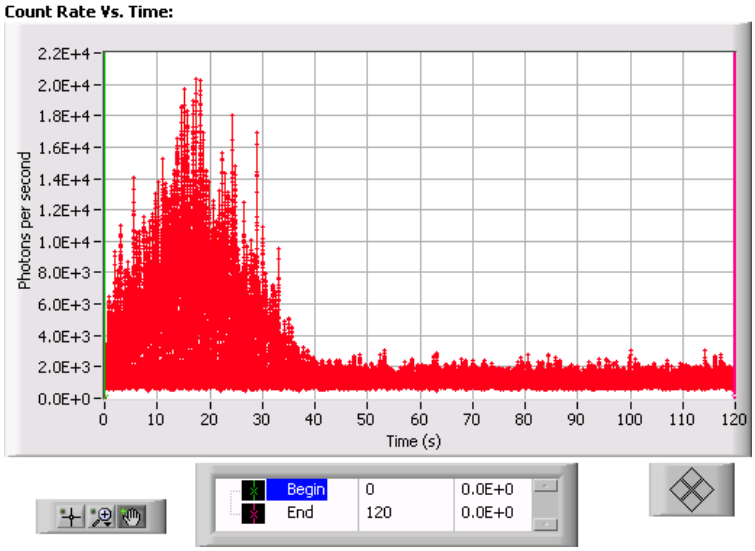

Figure 16. Count rate vs. time of raster scanning Nanogold on a quartz surface

5.2 Time Spectra

Time spectra data were taken for each sample using the procedure outlined in Section 4.5.2. The time spectrum for latex beads shown in Figure 17 took ~4.5 ns to fall to half the maximum value. The decay time was much longer than the 3.3 ns delay time between pulses. The time spectrum of the Rhodamine B in Figure 18 decayed to half the maximum value in ~1.5 ns, which is under the delay time between pulses. Figure 19 shows the Nanogold decay in a similar fashion. Both the Nanogold and the Rhodamine B decayed to half maximum before the next laser pulse arrived and were suitable for use with this apparatus.

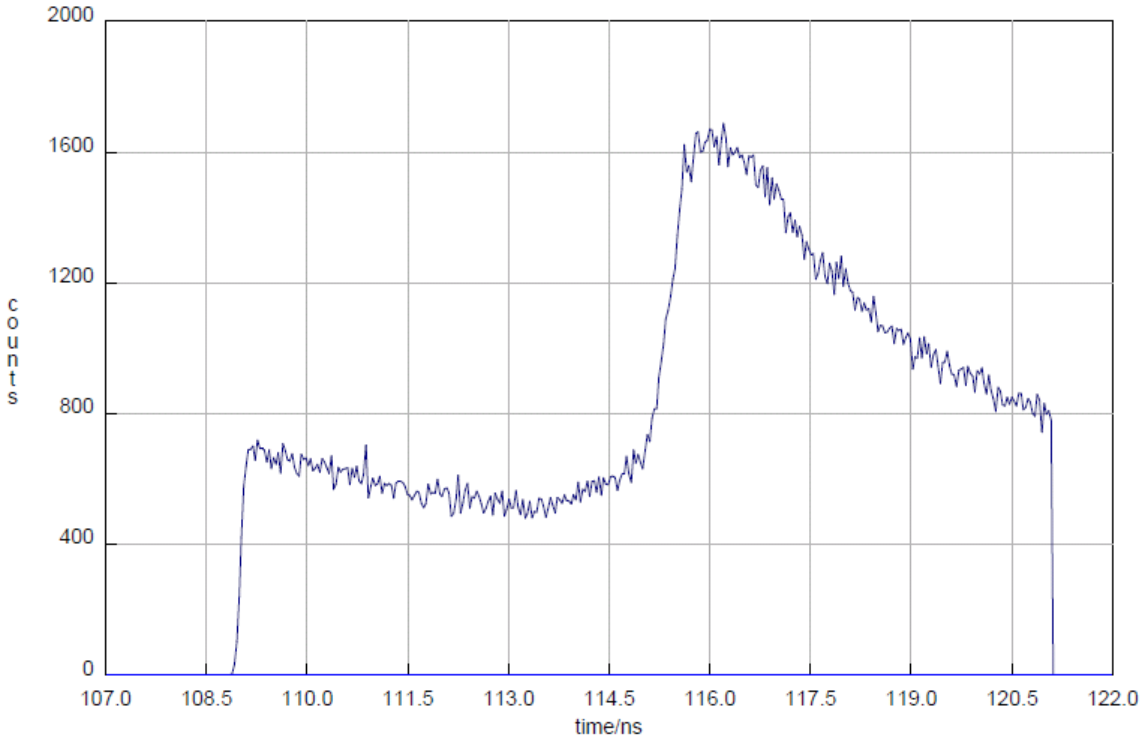

Figure 17. Time Spectrum of Latex Beads in water

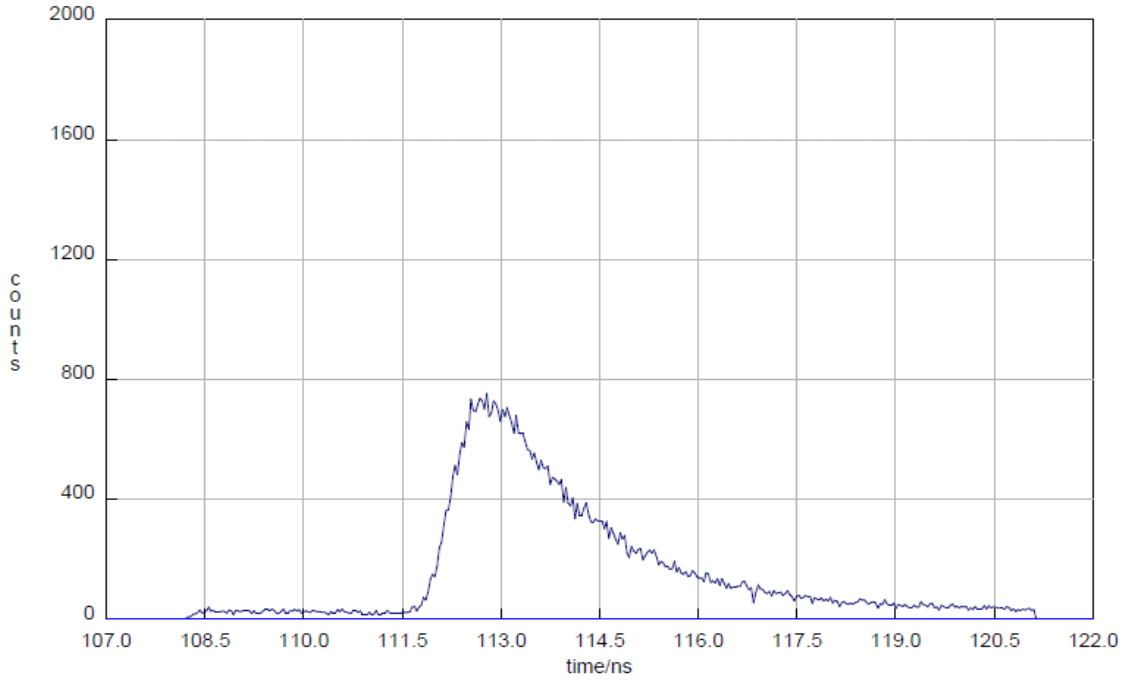

Figure 18. Time spectrum of Rhodamine B in water.

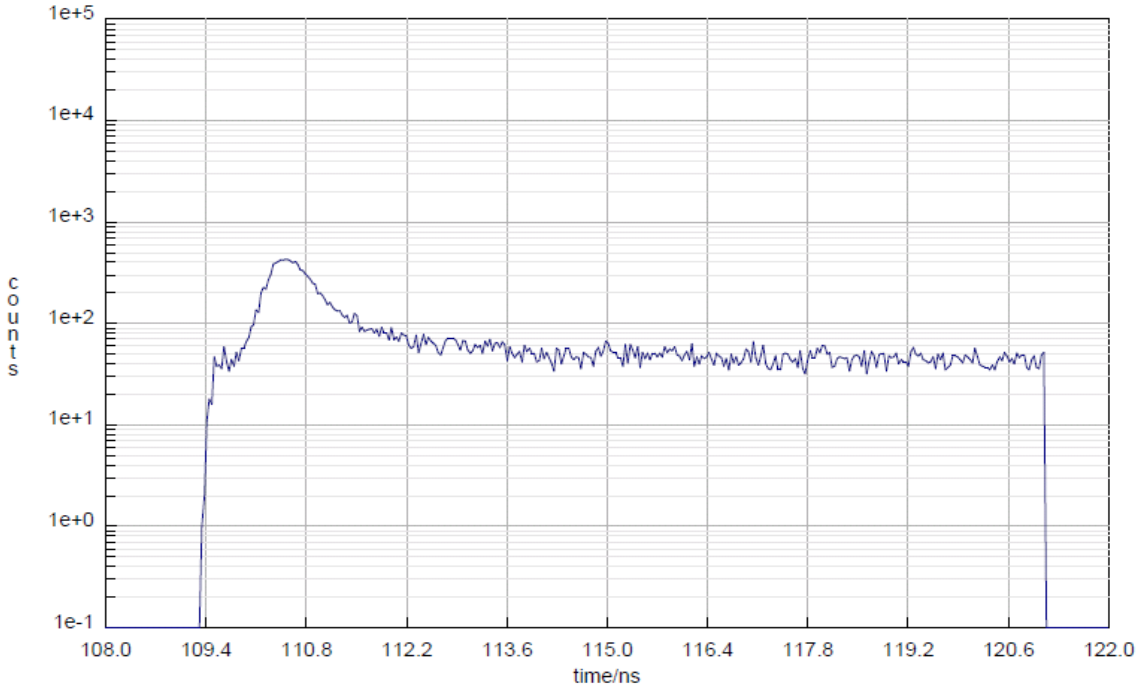

Figure 19. Time Spectrum of Nanogold in water

5.3 Diffusion through the Four Foci

Rhodamine B in water freely diffused through the four foci as described in the first paragraph of Section 4.5.3. With the Labview program "mainCorr" (described at the end of section 4.4), autocorrelation functions of the photons from each focus and the cross correlations of each focus with the other three foci were constructed. The autocorrelation and cross correlation functions are show in Figure 20 and Figures 21-24 respectively.

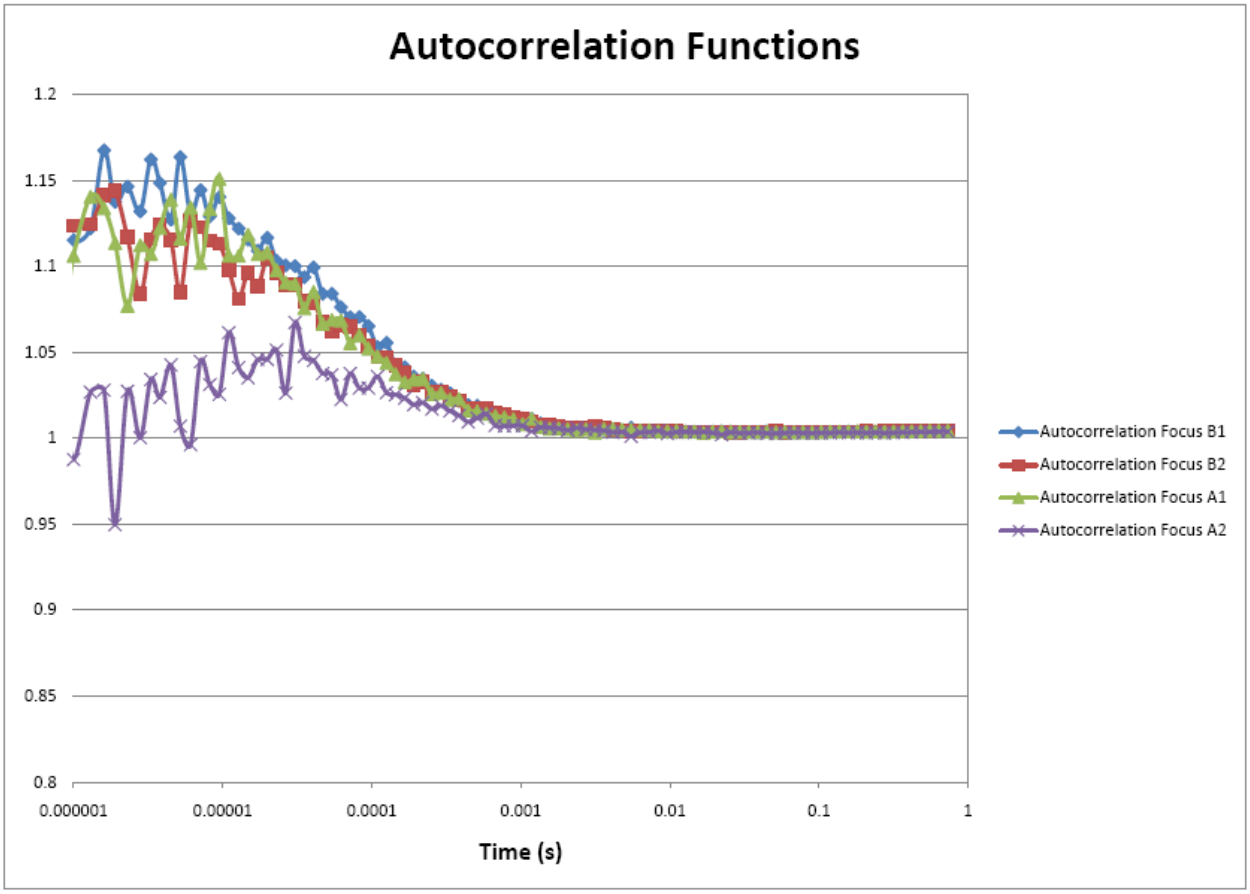

Figure 20. Autocorrelation functions of all foci

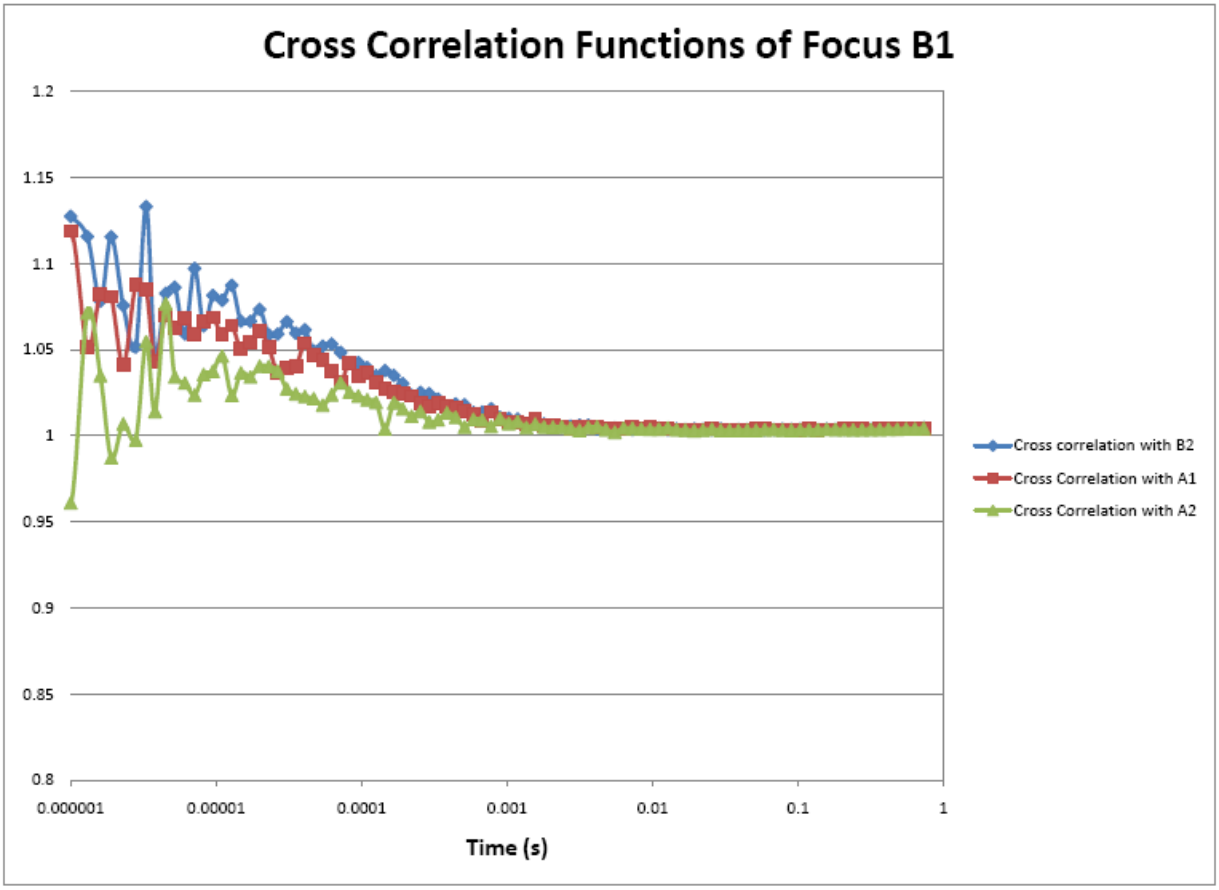

Figure 21. Cross correlation functions of focus B1

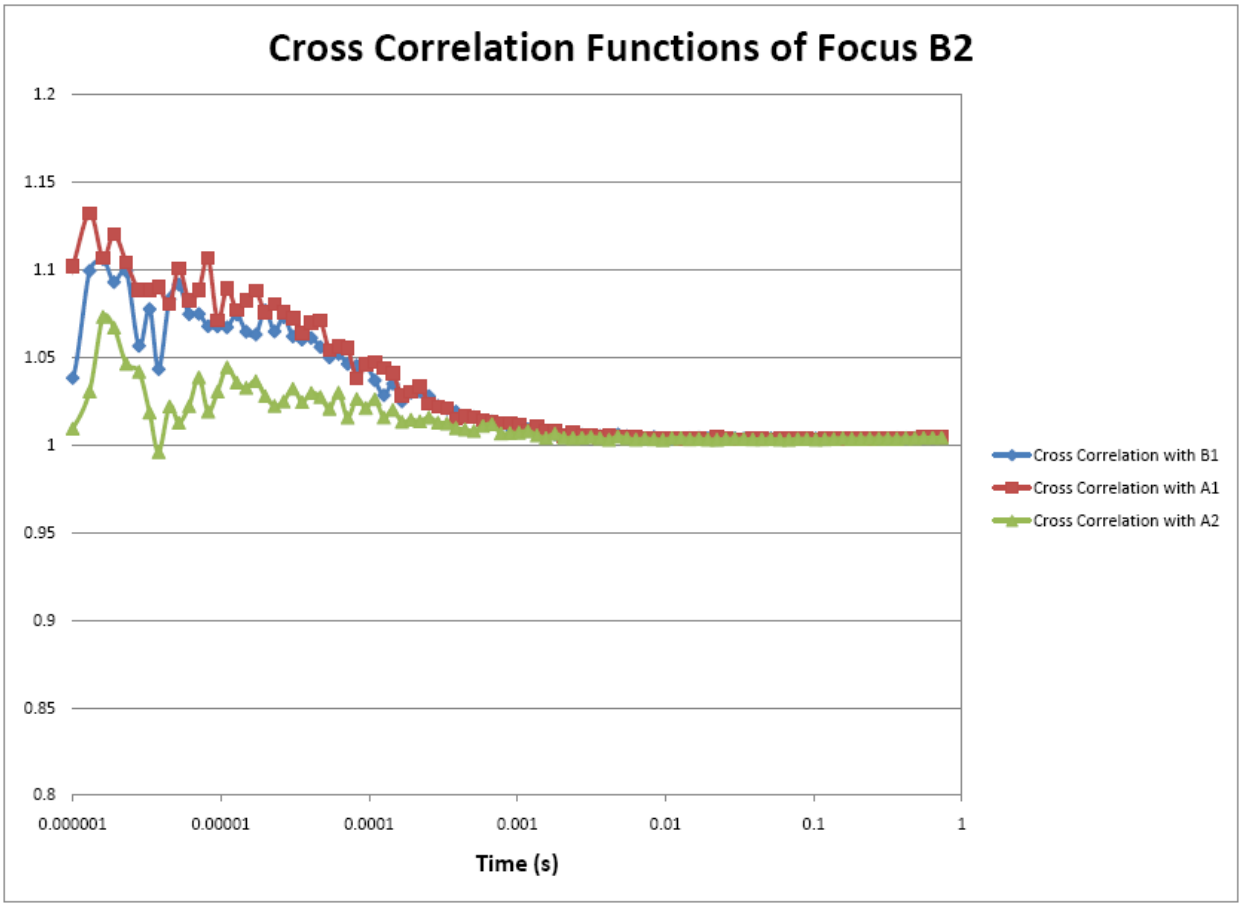

Figure 22. Cross correlation functions of focus B2

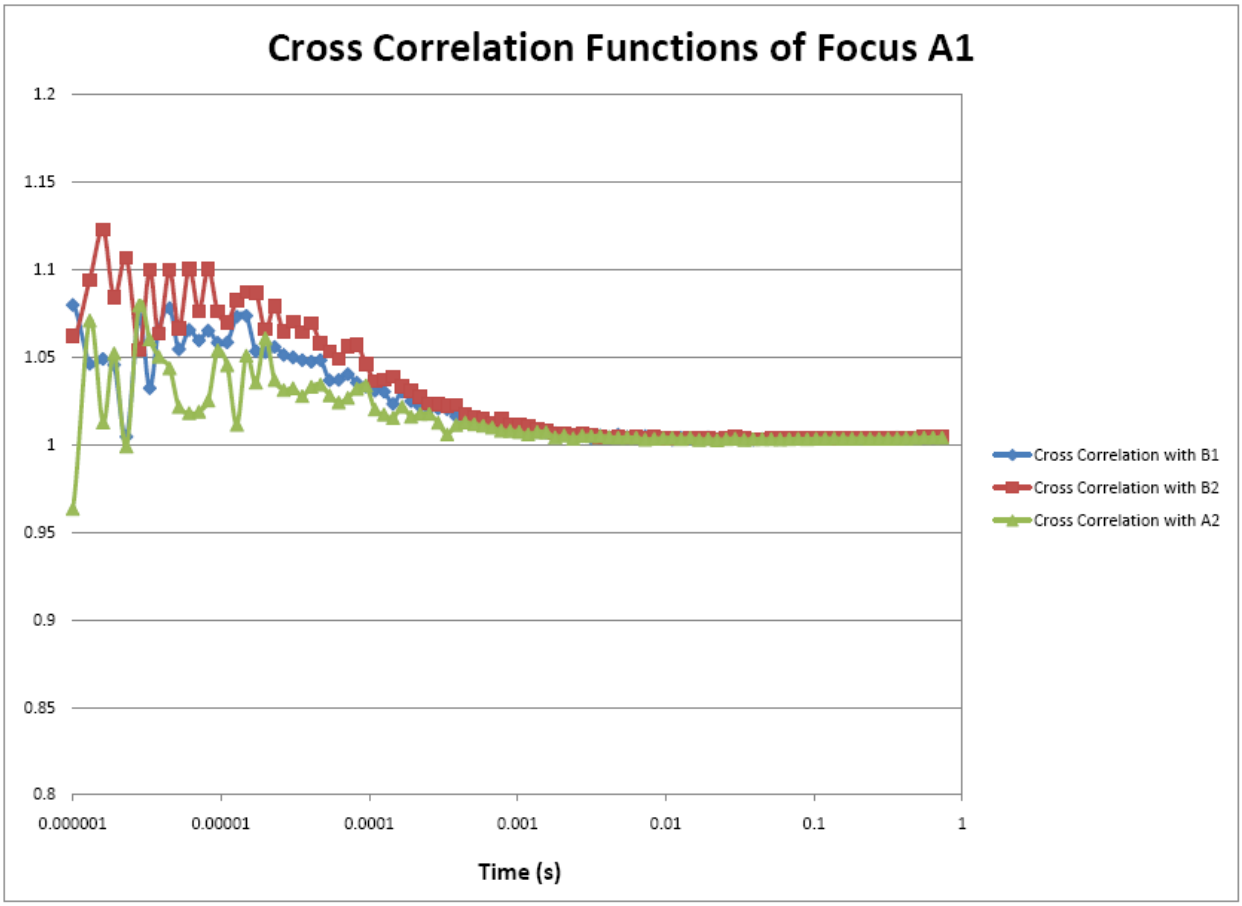

Figure 23. Cross correlation functions of focus A1

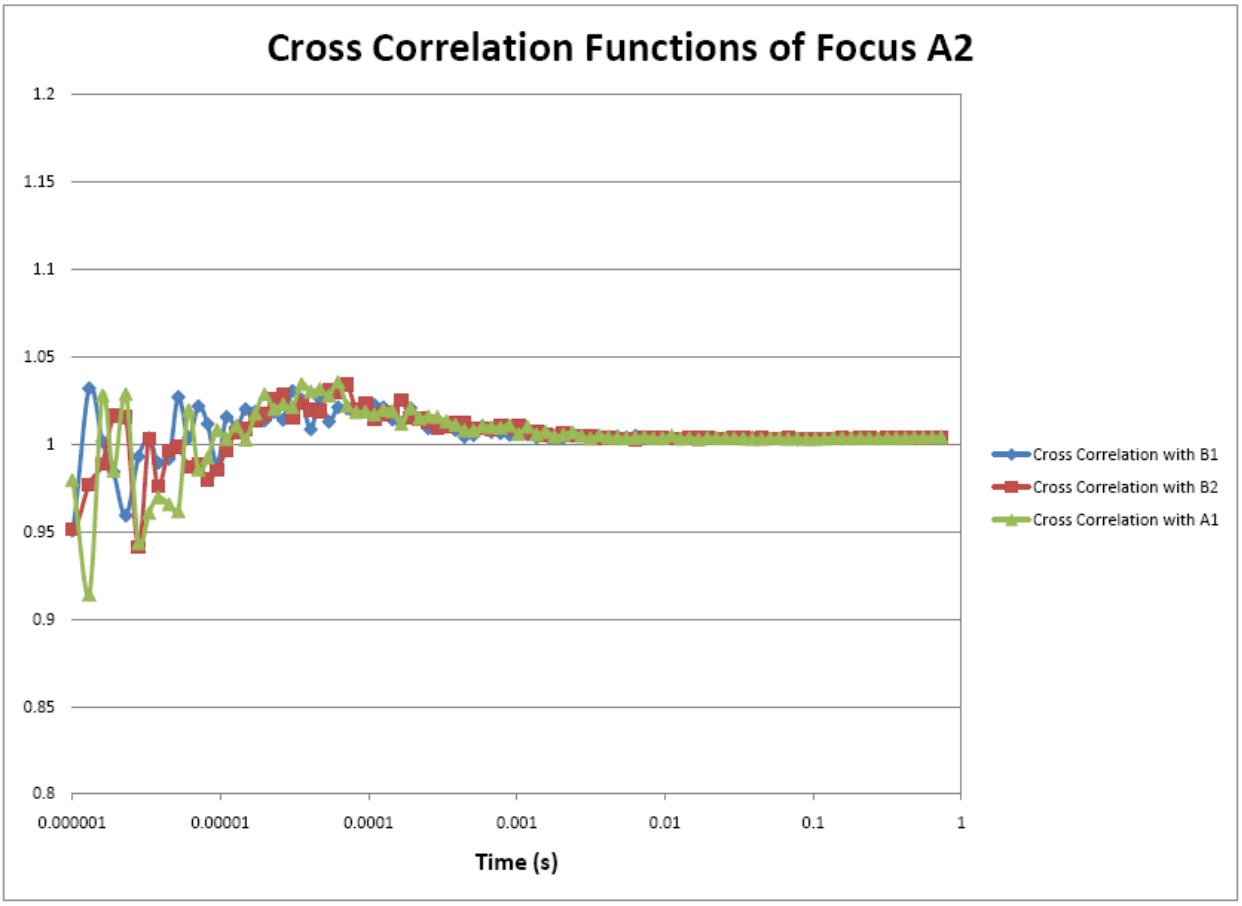

Figure 24. Cross correlation functions of focus A2

5.4 Raster Scanning Results

A limited number of Nanogold particles were raster scanned through the four foci as detailed in section 4.5.3. As the particles entered the beams, the emitted photon rate went up. The count rate during raster scan of each beam as shown in Figures 25—28 reveal similar count rate trends but not exactly the same count rate for each focus.

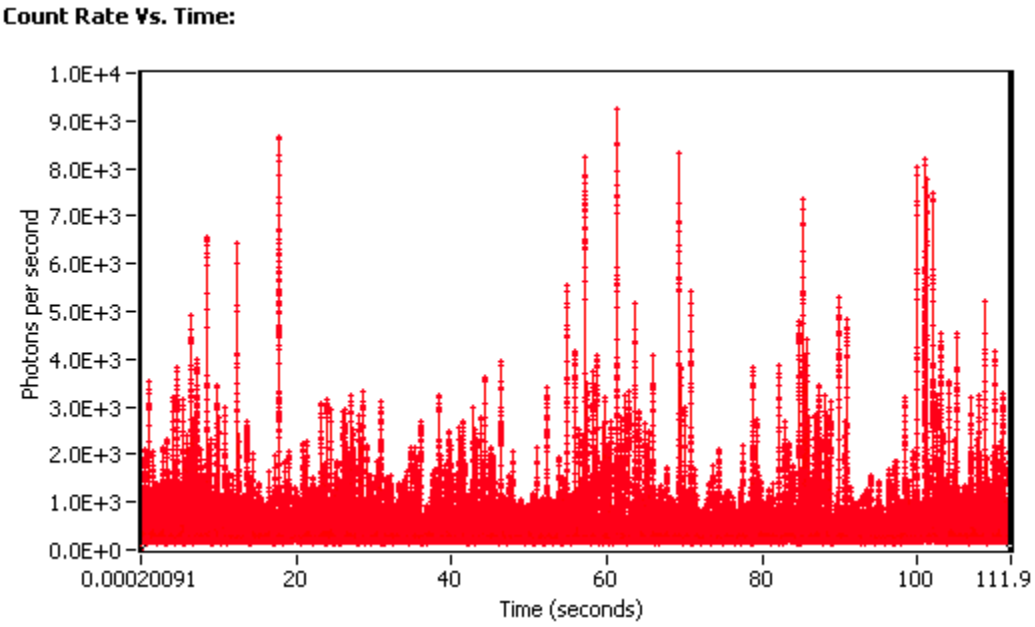

Figure 25. Raster scanning count rates of focus A1

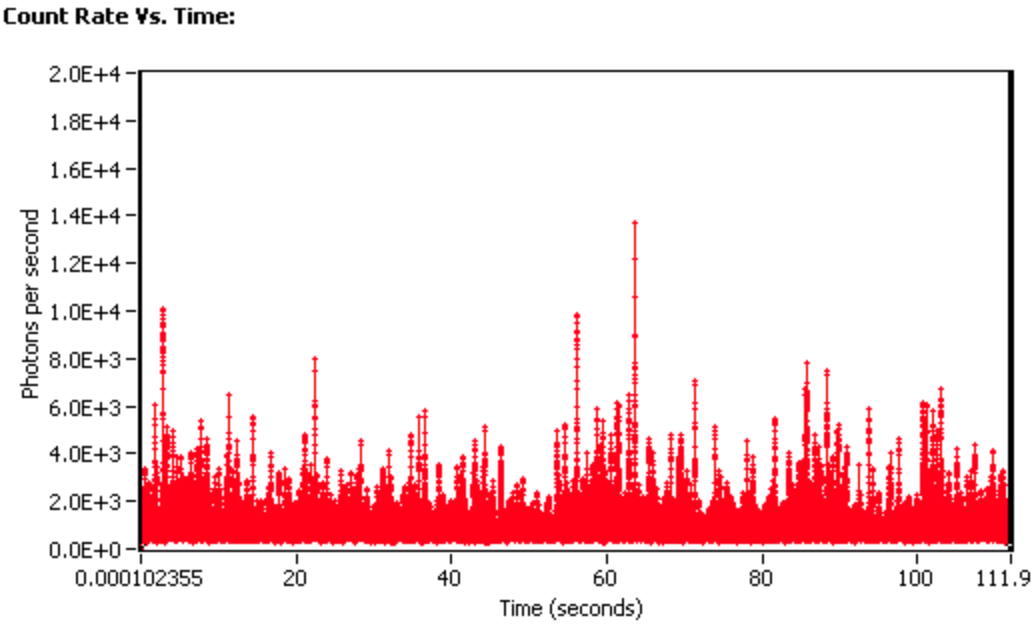

Figure 26. Raster scanning count rates of focus A2

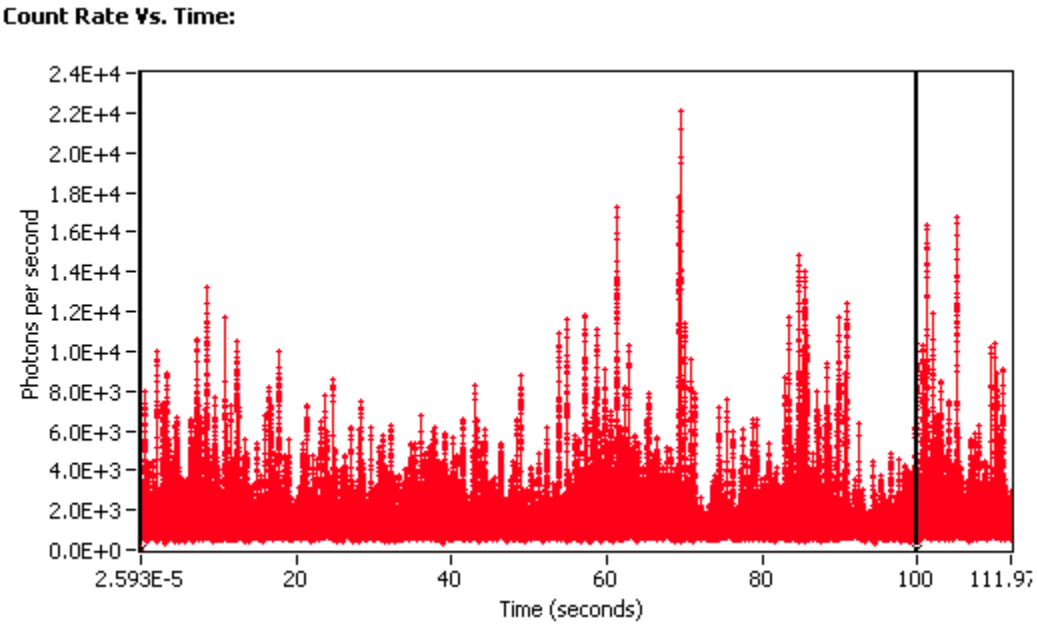

Figure 27. Raster scanning count rates of focus B1

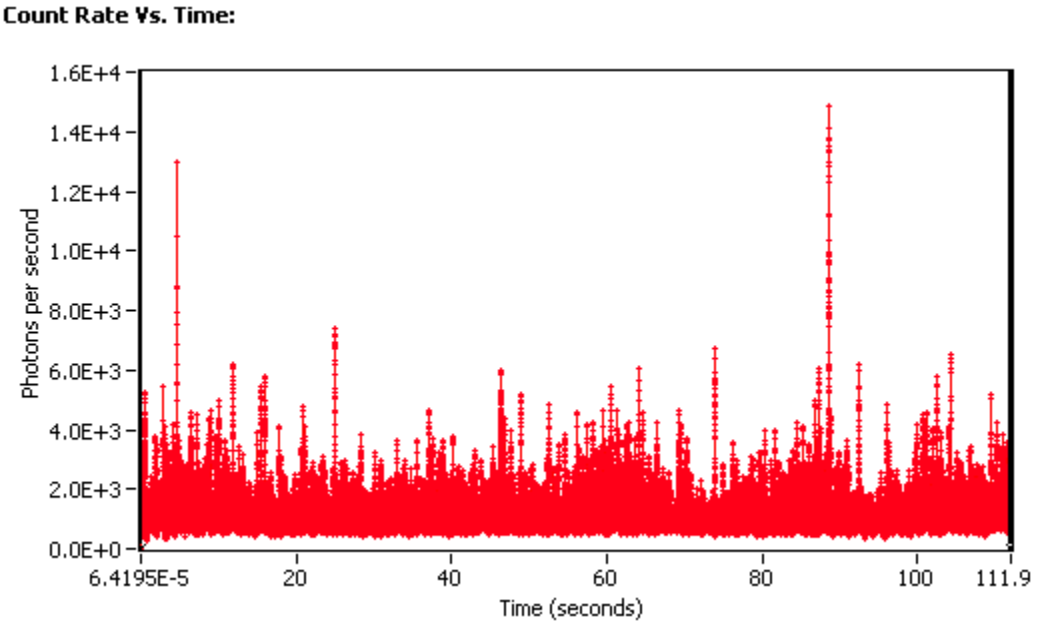

Figure 28. Raster scanning count rates of focus B2

6. Discussion

Three different samples were examined using the four-foci two-photon system; Rhodamine B, fluorescent latex beads, and Nanogold. Examination of the time decay and fluorescence correlation spectroscopy results eliminated latex beads as a viable sample to use in this apparatus, because the fluorescence created with one excitation pulse would often be binned in the wrong time bin. The gold beads in water failed to create an autocorrelation function, although raster scanning the gold beads on the surface of fused silica did result in higher count rates than in solution. The Rhodamine B in water and Nanogold on a surface had the best results. The FCS and time analysis experiments also showed that the apparatus is well aligned and sensitive enough to perform measurements on low concentration fluorescent molecule samples.

The autocorrelation and cross correlation functions of freely diffusing Rhodamine B match the expected model. The autocorrelation functions of A1, B1, and B2 had similar values and the cross correlation values matched a freely diffusing model. Focus A2 had a weaker signal-to-noise ratio as compared to the other three foci, as shown by the smaller amplitude of the autocorrelation. The cross correlation functions in relation to focus A2 also have noticeably lower amplitude compared to the other foci. This divergence could be attributed to aberrations in the focus A2 caused by alignment issues; possibly part of the beam was blocked by the optical mounts. Also, the laser powers for each of the four paths differed slightly and hence the addition of four adjustable neutral density filters to the four interferometer arms could possibly help to equalize the signals. Regardless of the possible issue with A2, the four-beam apparatus is capable of exciting a sample and each fluorescence photon can be detected and sorted according to

excitation focus. The raster scanning data confirms the ability to separate the photon counts from each focus by time-gated detection.

7. Conclusion

An apparatus based on the double Mach-Zehnder interferometer was constructed to create four spatially and temporally separated foci within a confocal microscope. Samples of Rhodamine B, Nanogold, and latex beads were examined using the apparatus to determine if they are viable candidates to use in localization experiments. Data indicate that the latex beads have too long of a decay lifetime to be used in this experiment and that the Nanogold does not provide sufficient signal when diffusing freely in water. Rhodamine B was selected to be used in solution to collect fluorescence cross correlation data from the four foci while Nanogold was dried onto a quartz slide, where the signal-to-noise was much greater, and raster scanned through the four foci. FCS measurements and raster scan data indicate that it is possible to group the excitation photons by excitation volume.

To improve the experiment, look up tables can be created to speed up the use of maximum-likelihood analysis for quick localization. The four foci would need to be traced with a single gold nanoparticle and the probabilities of position from focus intensity would need to be mapped out. Improvement can also be found in a stronger signal-to-noise ratio. Although the Nanogold provides extremely strong fluorescence signal when on the surface of a slide, in solution the signal is very weak. The signal from Rhodmaine B for two-photon processes in solution is adequate for FCS but the bursts from single molecules are weak. Research should be done to find a stronger fluorophore with a short enough lifetime to work with the 3.3 ns division between excitation pulses. Eventually, after the localization procedure has been optimized, a three dimensional flow control system could be used to control the position of the particle with feedback from the four-foci system.

List of References

[1] Thompson, Russell E., Daniel R. Larson, and Watt W. Webb. "Precise Nanometer Localization Analysis for Individual Fluorescent Probes." Biophysical Journal 82.5 (2002): 2775-2783.

[2] Speidel, Michael, Alexandr Jonáš, and Ernst-Ludwig Florin. "Three-dimensional Tracking of Fluorescent Nanoparticles with Subnanometer Precision by Use of Off-focus Imaging." Optics Letters 28.2 (2003): 69-71.

[3] Holtzer, Laurent, Tobias Meckel, and Thomas Schmidt. "Nanometric Three-Dimensional Tracking of Individual Quantum Dots in Cells." Applied Physics Letters 90.5 (2007)

[4] Ram, Sripad et al. "High Accuracy 3D Quantum Dot Trackingwith Multifocal Plane Microscopy for the Study of Fast Intracellular Dynamics in Live Cells." Biophysical Journal 95 (2008): 6025-6043.

[5] Pavani, SR P., and R. Piestun. "Three Dimensional Tracking of Fluorescent Microparticles Using a Photon-limited Double-helix Response System." Optics Express 16.26 (2008): 22048-22057.

[6] Moerner, W. E., and David P. Fromm. "Methods of Single-molecule Fluorescence Spectroscopy and Microscopy." Review of Scintific Instruments 74.8 (2003): 3597-3619.

[7] Enderlein, J. "Tracking of Fluorescent Molecules Diffusing within Membranes." Applied Physics B: Lasers and Optics 71.5 (2000): 773-777.

[8] Levi, V. et al. "Scanning FCS, a Novel Method for Three-Dimensional Particle Tracking." Biochemical Society Transactions 31 (2003): 997-1000.

[9] Wells, N. P., G. A. Lessard, and J. H. Werner. "Confocal, Three-Dimensional Tracking of Individual Quantum Dots in High-Background Environment." Anal. Chem. 80.24 (2008): 9830-9834.

[10] Davis, Lloyd M. et al. "Maximum-likelihood Position Sensing and Actively Controlled Electrokinetic Transport for Single-molecule Trapping." Procedings of SPIE 6862 (2008):.

[11] Elson, E. L., and D. Magde. "FLUORESCENCE CORRELATION SPECTROSCOPY .1. CONCEPTUAL BASIS AND THEORY." Biopolymers 13.1 (1974): 1-27.

[12] Lakowicz, Joseph R. Principles of Fluorescence Spectroscopy. : Springer, 2006.

[13] Mertz, J., C. Xu, and W. W. Webb. "Single-molecule Detection by Two-photon-excited Fluorescence." Optics Letters 20.24 (1995): 2532-2534.

[14] Berland, K. M., PT C. So, and E. Gratton. "2-Photon Fluorescence Correlation Spectroscopy - Method and Application to the Intracellular Environment." Biophysical Journal 68.2 (1995): 694-701.

[15] Denk, W., J. H. Strickler, and W. W. Webb. "2-Photon Laser Scanning Fluorescence Microscopy." Science 248.4951 (1990): 73-76.

[16] Myung, I. J. "Tutorial on Maximum Likelihood Estimation." Journal of Mathematical Psychology 47.1 (2003): 90-100.

[17] Spinelli, A., L. M. Davis, and H. Dautet. "Actively Quenched Single-photon Avalanche Diode for High Repetition Rate Time-gated Photon Counting." Review of Scientific Instruments 67.1 (1996): 55-61.

[18] Farrer, R. A. et al. "Highly Efficient Multiphoton-absorption-induced Luminescence from Gold Nanoparticles." Nano Letters 5.6 (2005): 1139-1142.

[19] Van Dijk, M. A. et al. "Absorption and Scattering Microscopy of Single Metal Nanoparticles." Physical Chemistry Chemical Physics 8.30 (2006): 3486-3495.

[20] Lee, Claudia Y., and Enrico Gratton. "Raster Image Correlation Spectroscopy with Nano Gold Particles on Cell Membranes." Biophysical Journal Supplement S (2007): 421A.

[21] Xu, Chris, and Watt W. Webb. "Measurements of Two-photon Excitation Cross Sections of Molecular Fluorophores with Data from 690 to 1050 Nm." Journal of the Optical Society of America B-Optical Physics 13.8 (1996): 481-491.

Vita

James Germann was born in Portsmouth, Ohio on July 17, 1984. He attended North Carolina State University from 2003-2007 and received his B. S. Physics with a minor in mathematics.